A Small-Scale Model of Sea Ice Dynamics in the Antarctic Marginal Ice Zone Using Fluid-Structure Interaction and the Reference Map Technique.

Prepared by:

Nadiya Mahomed

Supervisors:

Prof. Sebastian Skatulla, Dr. Alfred Bogaers and Prof. Chris Rycroft

Thesis submitted in partial fulfilment of the requirements for the degree of

Master's of Science in Engineering

Department of Civil Engineering
Polar Engineering Research Group
Computational Continuum Mechanics Group
University of Cape Town, Private Bag Rondebosch, 7700
South Africa

Abstract

Sea ice covers approximately 10% of the Earth's surface and modulates the sea-air heat and momentum exchange, therefore playing a major role in the global climate. The Antarctic marginal ice zone (MIZ) is the seasonally varying region between the open Southern Ocean and the Antarctic pack ice. It is a highly dynamic area containing ice floes (highly mobile round pancake ice) surrounded by interstitial grease ice, where turbulent sea states prevent sea ice consolidation. The sea ice dynamics of this region influences the global climate and therefore research in this area is important to understand global climate and predict long-term change.

Adequate research on the region has been challenging due to its complex nature. Understanding sea ice dynamics processes and influence on global climate is complex and many simplifications have been made when modelling and analysing the system on a large scale. Many climate models struggle to encapsulate the regional and temporal variability of Antarctica. Positive and negative trends found by the models are influenced by statistical analyses chosen, with different methods producing opposing trends in some instances. Subsequently, there is less consensus on the accuracy of large-scale models. Large knowledge gaps still exist with regards to the natural variability of Antarctic sea ice, thus limiting the ability to accurately forecast long-term changes.

The accurate modelling of the interplay of temperature, waves, sea ice dynamics as well as wind and ocean currents is necessary, not only to predict sea ice dynamics and wave energy dissipation, but also to advance understanding of the governing mechanisms of sea ice growth and decay in the Antarctic MIZ in particular. Deeper into the Antarctic MIZ with up to 100% sea ice concentration, the wave-ice interaction is highly complex being characterized by floe collision, turbulent eddy generation at the ice-water interface due to skin drag, and floe-grease ice interaction. Large- and mesoscale sea ice dynamics models are mainly continuum models and do not address the detailed heterogeneous sea ice composition. Finer-scale models on a floe level commonly use either a molecular dynamics schemes based on Hertzian collision dynamics or the discrete-element method. These models generally describe solitary ice floes floating in water as a collection of interacting particles, which, however, simplifies the ice floe solid mechanics behaviour and the fluid-structure interaction significantly.

In contrast to discrete particle models, this work proposed to study ice floe motion due to wave action. This is accomplished by developing and implementing a continuum approach for the solid and fluid constituents that accounts for the actual heterogeneous ice cover composition in terms of a geometrical layout of ice floes and interstitial grease ice. The model includes the respective material properties describing the solid-like deformation behaviour of ice floes and the fluid-like viscous behaviour of grease ice represented with their respective material laws. A novel fluid-structure interaction (FSI) method is employed, using the reference map technique (RMT), which accurately describes the interaction between the solids and fluid, and the response to wave forcing.

Plagiarism Declaration

- I know that plagiarism is wrong. Plagiarism is to use another's work and to pretend that it is one's own.
- Each significant contribution to and quotation in this document from the work or works of other people has been attributed and has been cited and referenced.
- This thesis is my own work.
- I have not allowed and will not allow anyone to copy my work with the intention of passing it as his or her own work.

Full Name: Nadiya Nazeema Joy Mahomed Student Number: MHMNAD014

Date: 05/06/2024 Signature: Signed by candidate

Acknowledgements

I would like to acknowledge my supervisors for the knowledge and experiences that they have shared with me over the last 25 months. Firstly, I would like to thank Prof. Sebastian Skatulla for offering his research topic to me and inviting me to join the Polar Engineering Research Group along with Dr. Keith MacHutchon. Prof. Skatulla also introduced me and gave me the opportunity to work with Dr. Alfred Bogaers, and to later collaborate with Prof. Chris Rycroft.

I would like to extend my thanks to Prof. Skatulla for his invaluable assistance in the continuum mechanics components of my thesis and for sharing his extensive knowledge and expertise of the Antarctic MIZ. Thank you for also allowing me to sit in on your continuum mechanics course, to improve my understanding and grasp of the topic.

I would like to thank Dr Alfred Bogaers for spending countless hours coding with me and explaining various computational techniques. Thank you for pointing me in the right direction with modelling in general, and modelling in FEniCS in particular.

One of the biggest honours was to meet and work with Prof. Chris Rycroft. I would like to thank Prof. Rycroft for inviting me to be a short-term research scholar at the University of Wisconsin-Madison, USA, and for partly funding my stay. Thank you for spending countless hours of coding from scratch with me to produce the model that we currently have. You have not only exposed me to amazing academic experiences and environments, but have also allowed me to experience travelling across the USA with you, and meeting other researchers in the field. This experience has been invaluable to me, both academically and personally.

I would also like to extend my thanks to Yue Sun, for her help building and troubleshooting the code when I had problems with it, while in the USA.

Thank you to Rutger Marquart and Thabang Lemphane for their assistance and explanations with the FSI problem at hand. I would also like to thank James MBewu for his assistance in editing and checking the mathematical components of my work, ensuring the grammatical and mathematical cohesiveness of my thesis.

Thank you to the National Research Foundation for funding my masters studies and to the University of Cape Town for partly funding my travels to the USA.

Finally, I would like to thank my peers and family who have supported me and helped edit my various drafts. Thank you to my peers for their moral support and assistance with reviewing my thesis in its final stages, and thank you to Meghan McClarty for her editing assistance. Thank you to my family for their lifelong support and thank you in particular to Hassan Mahomed for his assitance in reviewing my literature review.

In summary, I'd like to acknowledge and thank the following for their support and guidance through my thesis:

- Sebastian Skatulla
- Chris Rycroft
- Alfred Bogaers
- Keith MacHutchon
- James MBewu
- Rutger Marquart
- Thabang Lemphane
- Yue Sun
- Hassan Mahomed
- Meghan McClarty
- Zaid Karjikar
- Samir Koovarjee
- National Research Foundation
- University of Cape Town
- University of Wisconsin-Madison

Table of Contents

Abbreviations

AAIW	Antarctic Intermediate Water
ACC	Antarctic Circumpolar Current
ALE	Arbitrary Lagrangian-Eulerian
AOGCMs	Atmosphere-Ocean General Circulation Models
ASL	Amundsen Sea Low
BCs	boundary conditions
CFD	computational fluid dynamics
CFL	Courant-Friedrichs-Lewy
CMIP5	Coupled Model Intercomparison Project Phase 5
CPU	central processing unit
CSM	computational solid mechanics
DN	Dirichlet-Neumann
ENSO	El-Nino/La Nina Southern Oscillation
EVP	elastic-viscous-plastic
FEM	finite element modelling
FSI	fluid-structure interaction
GCMs	General Circulation Models
IBM	immersed boundary method
I-FEM	immersed finite element methods
IPCC AR4	Intergovernmental Panel on Climate Change's Fourth Assessment Report
MIZ	marginal ice zone
RMT	reference map technique
SAM	Southern Annular Mode
VP	viscous-plastic
WAP	West Antarctic Peninsula

Nomenclature

$\boldsymbol{\chi}$	Deformation map
$\boldsymbol{\sigma}$	Stress tensor
$\boldsymbol{\xi}$	Reference map
$\boldsymbol{\zeta}$	Internal solid state variable
$\boldsymbol{F}$	Deformation gradient tensor
$\boldsymbol{g}$	Gravitational acceleration (m/s^2)
$\boldsymbol{I}$	Identity matrix
$\boldsymbol{T}$	Boundary traction
$\boldsymbol{u}$	Velocity (m/s)
$\boldsymbol{v}$	Vector test function
$\boldsymbol{X}$	Reference coordinate system
$\epsilon(u)$	Strain rate tensor
ϵ	Wave height parameter (m)
μ	Dynamic viscosity
ω	Wave frequency ($/s$)
$\phi(\boldsymbol{x}, t)$	Level set function
ϕ	Bulk potential function
ψ	Drag coefficient
ρ	Density (kg/m^3)
φ	Restriction of the velocity potential to the free surface
c_c	Compressive wave speed
c_s	Shear wave speed
G	Shear modulus
H	Grid refinement
h	Element spacing (m)
h_x	Element width
h_y	Element height

j, k	Complex numbers representing wave numbers
K	Bulk modulus
L	Domain length (m)
p	Pressure
t	Time (s)
W	Domain width (m)
η	Height of ocean surface over time (m)
J	Jacobian matrix
q	Scalar test function

List of Figures

List of Tables

Chapter 1

Introduction

1.1 Background

The Antarctic marginal ice zone (MIZ) is the region between the open Southern Ocean and the pack ice of Antarctica [48, 49]. It is a highly dynamic area containing ice floes surrounded by grease ice whose size varies seasonally [22]. The sea ice dynamics of this region influences the global climate due to the large surface area it occupies relative to the Earth's surface [22, 23], thus research of this area is important to understand the global climate and possible changes thereof.

According to Mosig, Montiel, and Squire [25], contemporary climate models are only partially accurate in forecasting changes in trends as some important physical processes are neglected. This is shown by Maksym [20] where the global climate models failed to accurately model the increase in Antarctic sea ice extent which had been observed over the past several decades, and rather produced a modest decrease in extent. Furthermore, the models predicted that the areal extent of the Antarctic sea ice will be reduced 24% by the year 2100 [2, 23]. Since these models were tracking global sea ice extent and thickness, large discrepancies across the eleven models studied were found, due to the many simplifications made on the sea ice dynamics [22, 23, 26].

Many climate models struggle to encapsulate the regional and temporal variability of Antarctica including the winter expansion and summer retreat timing [48]. The positive and negative trends found by the models are influenced by the statistical analyses chosen, with different methods producing opposing trends in some instances [48]. Further confusion was created from satellite data which recorded a decrease in Antarctic sea ice extent in 2016, whereas in previous years, an increase in extent was recorded [8, 20]. The degree of consensus on large-scale models has thus reduced [20, 48]. Vichi [48] states that large knowledge gaps still exist with regards to the natural variability of Antarctic sea ice. Moreover, climate models have struggled to robustly simulate the forced and natural variability that has driven changes in both the Arctic and Antarctic regions thus limiting the ability to forecast long-term future changes [20].

It is therefore evident that more accurate models are required to ensure better small-scale and large-scale climate predictions [22]. A more accurate model of the small-scale sea ice dynamics and ocean-ice interactions may contribute to more accurate global climate models [20, 23, 48]. An increasing number of researchers are assessing the use of Fluid-Structure Interaction (FSI) to confront complex multi-physics problems and systems characterised by interacting physical processes which were previously solved separately [38]. A system such as sea ice dynamics falls into this category.

1.2 Research Problem

The seasonal sea ice advance and retreat of the Antarctic is one of the main contributors to the albedo and physical variations on the globe, including sea level rise[14]. Adequate research on the region has been lacking due to its complex nature, especially in relation to modelling and predicting sea ice behaviour [23]. Understanding sea ice dynamics processes, interactions and influence on global climate is complex and many simplifications have been made when modelling and analysing the system on a large scale [23, 25].

A numerical technique that combines computational fluid dynamics (CFD) and computational solid mechanics (CSM), called FSI, can be used to simulate the interaction of solids and fluid [3]. Such a technique may provide a more accurate solution to sea ice dynamics when modelling grease ice as the fluid and ice floes as solids. Both solid and fluid material properties can be accurately modelled and the coupling between the constituents can be computed with various coupling schemes, therefore simultaneously providing accurate results of both fluid and solids [37]. Computational results generated will inform the pressure, velocity, stress, strain, and strain rate response of both the fluid and solids [22, 37].

This research creates and simulates a proof of concept for a novel small-scale sea ice dynamics FSI model using the reference map technique (RMT). It represents the behaviour and interaction of both solid ice floes and fluid-like grease ice in the Antarctic MIZ. This work is necessary to aid the investigation on the influence of sea ice dynamics on annual ice growth and retreat in the Southern Ocean which, in turn, will help to improve global climate models.

1.3 Research Questions

Based on the above problem, the research aims to address the following questions:

1. How can FSI be used to simulate sea-ice dynamics?
2. Which factors contribute to the sea ice dynamics?
3. How can free-floating structures be modelled using FSI?
4. How can FSI be used to simulate grease ice-ice floe interactions?
5. How does the RMT provide an alternative approach to modelling sea ice dynamics?

1.4 Research Objectives

The research aimed to develop a proof of concept model using FSI and the RMT which can be used to describe the sea-ice dynamics and rheologies in the Antarctic MIZ. The research aims to achieve the following objectives:

1. Develop, implement and calibrate a small-scale two-dimensional FSI model.
2. Model solid ice floes that are free-floating relative to the surrounding grease ice.
3. Study the stress, strain and strain rate response of ice floe-grease ice interaction and dynamics when subjected to traction/drag forces and wave forcing.
4. Provide a new improved modelling technique for sea ice dynamics of solitary ice floes and multiple ice floes in a viscous fluid domain as applicable for the MIZ.

1.5 Scope and Limitations

This study will focus on creating a two-dimensional small-scale model which represents a 'bird's-eye-view' of sea ice dynamics found in the Antarctic MIZ. It will make use of FSI techniques to accurately model interactions of the ice floes and grease ice. The following concepts will be focused on:

- Simulating two-dimensional free-floating ice floes in grease ice using FSI and the RMT.
- Compressible neo-Hookean hyperelastic material framework for solids.
- Wave forcing of the grease ice transferred to the solid ice floes.
- Navier-Stokes flow with Newtonian material law for fluids.
- Recording solid and fluid stresses, velocity and strain rate responses of the ice floe-grease ice interaction.

To contribute to making this type of research more accessible to the scientific community, open-source computational modelling software will be used.

The following concepts will not be studied due to time constraints and credits allocated for a 180-credit master's thesis:

- The inelastic collisions.
- Friction between ice floes, and between ice floes and the grease ice.

- Self-adhesion of the floes.
- Three-dimensional simulations of sea ice dynamics.
- Large-scale modelling of sea ice dynamics.

Chapter 2

Literature Review

2.1 Ice Cover and the Global Climate

Polar oceans cover 7% of the planet, an area larger than the combined surface area of Europe and North America [49]. Ice-covered seas contribute to the ocean's heat regulation system which has enabled the Earth to support various life forms, including human life [49]. Sea ice serves an important regulatory function in the global climate as its extent, ice cover consistency, and thickness are responsible for the removal of heat due to solar radiation [49].

Sea ice and snow covered regions, due to its albedo, reflect approximately 80-90% of incident solar radiation, compared to that of open water which only reflects approximately 10% [49]. According to Massom and Stammerjohn [23], sea ice is relatively sensitive to climate change and variability, but sea ice itself is also responsible for such change through the systems such as the ice-albedo feedback system. When sea ice cover reduces due to climate warming, increased radiation is absorbed by the Earth and subsequently, the rate of warming increases, which, according the global climate models, increases the rate of global climate change [14, 49].

As the ice cover grows, it increases salt/brine rejection into the ocean. The surface water in the polar regions becomes more dense and is able to transport oxygen and dissolved carbon dioxide (CO_2) into deeper parts of the ocean, thus making life possible in deep parts of oceans all around the world [49]. This convection occurs on the Arctic Ocean continental shelves, the Greenland Sea and the Antarctic Ocean, all of which drive a global pattern of ocean currents called thermohaline circulation (or the "Great Ocean Conveyor Belt") [49].

A review by Maksym [20] compares the Arctic with the Antarctic, noting that the overall global sea ice cover is strongly decreasing. Over the past couple of decades, there has been a notable decline in Arctic ice and high temporal and regional variability in the Antarctic [20]. Researchers pose the question of how much of these changes in ice cover is due to natural climate variability and how much is due to the expected response of a warming global climate [20]?

Sea ice and snow cover represent the largest seasonal changes in the appearance of the Earth and it is regarded as an important component in understanding the energy balance of the Earth [44]. Antarctica specifically has a highly variable and dynamic influence on the global climate as well as marine life in high-latitude ecosystems due to the large cycles of sea ice growth and decay every year [23, 49].

In order to predict the effects of radiative forcing on the global climate, a series of General

Circulation Models (GCMs) have been developed by university groups and meteorological institutions across the world [49]. These large-scale models take into account the climate system feedback mechanisms which affect the amount, rate and geographical location of global warming [31]. According to Wadhams [49], the four most important feedback mechanisms are water vapour feedback, cloud-radiation feedback, ocean circulation feedbacks, and ice-albedo feedback.

Two categories of models were developed, equilibrium models and time-dependent models. Equilibrium models consider the effect on radiation due to doubling CO_2 concentration and then allowing the climate to reach an equilibrium. These models predicted surface warming at high northern and southern latitudes, both greater than the global average in winter yet smaller in summer. They also predicted an increase in precipitation, with a greater increase where the warming is larger, and a decrease in sea ice area and seasonal snow cover. Such models are unrealistic, because they do not allow for time-dependent responses such as ocean circulation feedbacks which slow the rate of warming in oceanic regions due to the oceans' heat capacity [49]. Thus time-dependent models have replaced equilibrium models. These models add CO_2 at a realistic rate and have rate-dependent responses. They produced results which were qualitatively similar to the equilibrium models, but at high southern latitudes, the models predicted a very small amount of warming due to the large influence of the Southern Ocean [49]. The models predicted that in 80 years, the arctic regions would experience an increase of 4.8 °C to 6.5 °C whereas the Antarctic region would only experience a 1.2 °C increase in the same time frame [49]. Wadhams [49] comments that using global coupled models for regional predictions still has a relatively low confidence.

GCMs have shown large discrepancies in their predictions for the Antarctic. Early equilibrium models (performed in 1988) predicted an equal amount of warming in the Antarctic Ocean as found in the Arctic, and even greater warming at lower latitudes. On the other hand, time-dependent models predicted that the Antarctic MIZ will experience the lowest rise in temperature compared to any other latitude across the globe, with less than a 1 °C increase in a span of 60 years [49]. Furthermore, observational data on sea ice extent in the Antarctic has shown no significant trend. A long-term statistical analysis of passive microwave data starting from 1978 produced a slight and statistically insignificant upward trend in Antarctic ice extent. Wadhams [49] concluded that the GCMs predictions and sea ice extent analyses agree in showing no significant trend in the Antarctic.

A study by Arzel, Fichefet, and Goosse [2] compares 15 different Atmosphere-Ocean General Circulation Models (AOGCMs) for the Intergovernmental Panel on Climate Change's Fourth Assessment Report (IPCC AR4) to examine sea ice evolution over the 20th and 21st centuries. The models compared in the study were: IPSL-CM4, CNRM-CM3, GISS-AOM, FGOALS-g1.0, CSIRO-Mk3.0, INM-CM3.0, UKMO-HadGEM1, UKMO-HadCM3, MRICGCM2.3.2, GISS-ER, MIROC3.2 (hires), CCSM3, MIROC3.2 (medres), CGCM3.1 (T47), PCM [2]. Models were assessed on their ability to reproduce observed sea ice changes in northern and southern hemispheres during 1951-2000 and 1981-2000, and the different models' sea ice projections

for the 21st century were compared [2]. The analysis is based on the simulated trends, the standard deviations of sea ice extent and volume, and geographical distribution of ice thickness and concentrations [2]. Firstly, the 20-year period (1981-2000), taken from the most reliable observations of the output of the "Climate of the 20th Century Experiment" (20C3M), was used to assess the 15 AOGCMs. The average March and September sea ice extents and annual mean changes of sea ice volume and extent were computed for each ensemble simulation of each model in both hemispheres over the observed period. The results of each simulation were then averaged for each model. Arzel, Fichefet, and Goosse [2] define sea ice extent as the total area of oceanic grid boxes with an ice concentration of more than 15%. Two models, the INM-CM3.0 and CSIRO-MK3.0, produced errors smaller than 10% relative to the observational data in the late summer in the Southern Hemisphere; and in late Antarctic winter, seven models produced errors smaller than 10%. Furthermore, the CSIRO-MK3.0 model is the only model of the 15 which has relative errors smaller than 10% for both late winter and late summer in the Southern Hemisphere [2]. Secondly, it was necessary to extend the research beyond the 20-year period to check if the conclusions were valid for longer periods of time. The analyses of the climatology over the period 1951-2000 provides similar conclusions about the models' strengths and weaknesses [2]. The multi-model ensemble mean sea ice trends in the Southern Hemisphere was not statistically significant with respect to the observations over 1951-2000 [2]. The annual mean sea ice volume trend from all the models shows a 5 times faster decrease in the Northern Hemisphere compared to the Southern Hemisphere, where the Northern Hemisphere result is significant with 95% confidence yet the Southern Hemisphere results are not statistically significant over the 50-year period [2].

The multi-frequency satellite passive microwave record started in late 1978. Massom and Stammerjohn [23] reviewed the large-scale sea ice distribution in Antarctica and its overall areal extent which is currently based on satellite data analyses during the period 1979-2006. In the Southern Ocean, sea ice has shown a statistically significant increase per decade of approximately 0.9% [23]. There is, however, substantial regional variability within the Antarctic circumpolar region, with strong apposing trends in the Amundsen-Bellingshausen Seas and the Ross Sea. Reasons for the contrast requires a more detailed examination of changes in the spatio-temporal aspects of of sea ice cover [23]. The main driver of observed spatio-temporal changes in sea ice cover in Antarctica is thought to be shifts, on a decadal-scale, in dominant modes of atmospheric circulation in the Southern Hemisphere. These are large-scale wind patterns with the most notable being the Southern Annular Mode (SAM) or Antarctic Oscillation, the high latitude response to the El-Nino/La Nina Southern Oscillation (ENSO), and the Wave 3 pattern [23].

Polvani and Smith [30] used four Coupled Model Intercomparison Project Phase 5 (CMIP5) models to show that the observed Antarctic sea ice trends are mainly due to natural variability and hardly due to anthropogenic forcings. The study analyses the pre-industrial integrations of the models as an experiment control and compare them to periods of time when anthropogenic forcings on the climate are present, specifically the period 1979-2005. The four suitable CMIP5 models used were: two models from the Community Earth System Model (CESM) project

(the Community Climate System Model Version 4 (CCSM4) and the Whole Atmosphere Community Climate Model (CESM1-WACCM)), and two Earth System Models (ESMs) from the Geophysical Fluid Dynamics Laboratory (GFDL) (GFDL-ESM2M and GFDL-ESM2G) [30]. The CESM and GFDL models were chosen because they make use of independently developed sea ice modules which allows a better assessment of the robustness of the results obtained. The models also allow for comparisons in natural variability to be made based on different biases in climatological Antarctic sea ice extent over a range of different model configurations. The two CESM models had identical sea ice and ocean components but different atmosphere components, and the GFDL models had identical sea ice and atmosphere configurations but different ocean components [30]. In addition to the CMIP5 data, three observational data sets on Antarctic sea ice were analysed: NASA/National Snow and Ice Data Centre (NSIDC), NSIDC/Bootstrap, and the Hadley Centre Sea Ice and Sea surface Temperature data set (HadISST), updated to 2005 [30]. As expected in a warming climate, the four models all produced larger sea ice extents in the pre-industrial integrations than the period 1979-2005. The trends of the sea ice extent observed in the 27-year period appear spontaneously in the absence of any kind of external forcing in all four models over a multidecadal time-scale (the models collected data for 200 to 500 years). The results suggested that the magnitude of the observed sea ice extent trend cannot be distinguished from naturally occurring multidecadal trends [30]. The latest Coupled Model Intercomparison Project Phase 6 (CMIP6), compared to the previous model generation (CMIP5), has a reduced sea ice area spread, and an improved regional distribution of sea ice concentration [34].

2.2 Antarctica and the Marginal Ice Zone

According to Wadhams [49], Antarctic sea ice cover is, climatically, one of the most important features of the southern hemisphere. Its maximum ice extent, which is circumpolar, occurs during August and September, and its furthest retreat occurs in February [49]. The impact of Antarctica on global climate depends on several factors such as the ice areal extent, sea ice dynamics, degree of deformation, sea ice concentration, type of ice, thickness distribution and snow cover [23].

The Antarctic sea ice trends, unlike the Arctic, have shown substantial variations between regions such as the Southern Amundsen and Bellingshausen Seas and the Western Ross Sea (refer to Figure 2.1) [20]. The changes in sea ice in the Bellingshausen Sea, northeast and West Antarctic Peninsula (WAP) are in contrast to that of the Ross Sea mainly due to changes in the wind direction [23]. Such changes in the direction of wind can be owed to anthropogenic climate change - that is climate change due to human activity [23]. In the WAP region, rapid decline in sea ice has affected the physical environment, marine ecosystems and food webs at various levels with the occurrence of complex compounding sea ice related events [23].

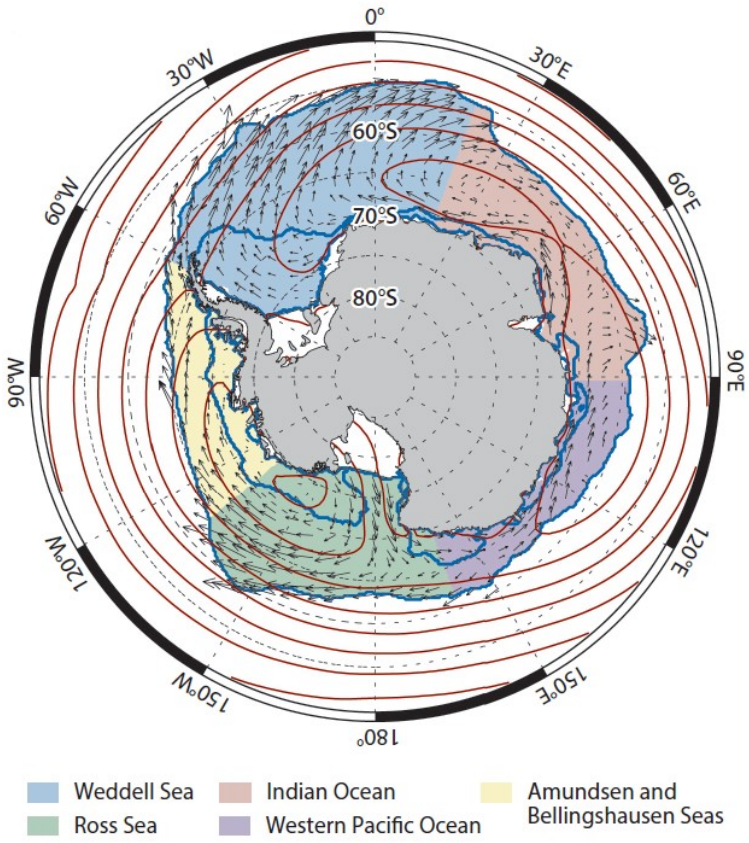

Figure 2.1: Map showing the different seas surrounding Antarctica, reproducted from Maksym [20].

The open nature of the Antarctic retreating ice cover, with divergent ice floes, is the major agent in allowing high light intensity under the ice cover. This allows for phytoplankton growth to occur, especially near the edge of retreating ice cover [49]. The consolidated pancake ice (explained in Section 2.3) provides a good substrate for phytoplankton and zooplankton due to the large surface area with voids and crevasses found on the underside of the overlapping masses. These crevasses provide zooplankton with protection from predators and attachment areas onto which the phytoplankton can grow [49]. Chlorophyll has been found throughout the depths of most ice cores analysed in Antarctica due to plankton being trapped in the grease ice (explained in Section 2.3) as it forms into pancakes and then into the first-year consolidated pancake ice sheet. This leads to potential seeding of surface water for plankton growth during melting seasons [49].

A dramatic marine ecosystem response has been observed in the WAP which has strong links to the change of sea ice and ocean circulation seasonality [23]. For example, reports of phytoplankton biomass from 1978-1986 and 1998-2006 show major changes due to changes in sea ice and wind patterns which has influenced the mixed-layer depth of the ocean, the area of open water and the availability of light [23]. It is expected that a significant decrease in the phytoplankton class size will be a recurring theme in the WAP region due to expected sea

ice loss and increased meltwater input from surrounding glaciers [23]. Phytoplankton is at the base of the food web for many marine organisms and thus directly or indirectly affects biota such as Antarctic krill, Adélie penguins and Antarctic silverfish [23]. Furthermore, studies from Ross et al. [35] and Massom and Stammerjohn [23] show that the timing of the sea ice expansion and retreat and the winter ice duration (known as seasonal sea ice dynamics) also affects the habitat quality for Antarctic krill. A shorter sea ice season negatively affects krill production but positively affects salps [35]. Salps are less nutrient rich source of food for higher predators and subsequently lead to a "dead end" in the food chain [23]. Sea ice deformation also affects the krill population, as thicker rafted ice provides more protection for young krill than thinner, undeformed ice [23].

Ocean structure, the distribution of water mass, ocean circulation and gas exchange between the air and the sea affect the oceans' biogeochemical cycling and ecosystem structure [23]. Recent evidence show trends of these aspects which lean towards a weaker Southern Ocean carbon sink [19] and increased ocean acidification [7], creating potential food web consequences [23]. Melting ice sheet margins and icebergs increase freshwater input which contributes to ocean stratification [23]. Changes in ocean stratification and sea ice distribution may experience drastic impacts on ocean circulation, ventilation and exchange of carbon between ocean and atmosphere which also affects ocean acidification [23].

The MIZ is the transition region between the consolidated ice and the open ocean, and the sea ice concentration ranges between 15% to 80% [29]. Antarctic sea ice area ranges from approximately 3 million km^2 in summer to 19 million km^2 in winter [6, 23] and has shown moderate increase in sea ice extent over the past few decades [20, 25]. During the summer, the ice edge retreats due to ice at the edge of the MIZ melting. As the ice edge retreats southwards, the net motion of the ice remains northwards and no new ice is formed. The consolidated pancake ice is broken into single ice floes by waves [49].

The width of the zone is defined as the distance into the ice where waves are still able to break up the ice into floes, and it is a function of ice thickness, mechanical properties and wave climatology [49]. Marginal ice zone characteristics are greatly determined by processes of ocean-wave-ice interactions [43]. In the outer edges of the MIZ, wave-ice interaction influences the sea ice formation, evolution, thickness distribution, concentration, floe size distribution and mechanical breakup and melt [23, 49]. Such interaction also contributes to the snow cover distribution and its properties, and the break up of fast ice, especially during the spring-summer transition [23]. The most amount of break-up occurs at the ice edge which produces the smallest ice floes [49]. The Antarctic MIZ is the longest and widest MIZ in the world (up to approximately 20 000 km long and 270 km wide) and faces the stormiest ocean on the planet during its winter [49]. The ice that forms at the stormy ice edge is frazil and pancake ice, and further into the MIZ where the waves are significantly damped, the pancakes may freeze together to form consolidated pancake ice [49]. Wave-ice interaction can also influence the pack ice due to long-period wave propagation [23]. When the waves are attenuated by the sea ice layer, consolidated ice cover forms; a process known as the pancake

ice cycle [29].

Wave-ice interaction plays a geophysical role, globally, in two ways: the physical effect of waves on ice cover; and the use of waves in ice mechanics as a diagnostic tool [49]. The physical effects involve the waves breaking up the ice sheets into ice floes and pushing the floes in patterns which determine the MIZ morphology [42]. As ice moves from the interior of the pack to the ice edge, it encounters an increasing wave energy and a decreasing peak wave period which increases the degree of flexure to vast ice sheets. The flexure eventually causes ice break-up, and the fragments continue to break into smaller pieces the closer to the ice edge they are. Thus, the smallest ice floes occurs at the ice edge where the wave field is steepest [49]. The ice floes which make up the MIZ act as a shield which protects the interior pack from destructive waves by damping out shorter waves [49]. The diagnostic role of wave-ice interaction comes from flexural-gravity waves, due to the long-range propagation of wave energy through ice sheets, from which information on dispersion relation and attenuation rates inform the ice mechanics and properties [49]. Deeper into the MIZ, where larger floes exist, the wave energy propagates as flexural-gravity waves and energy losses occur as reflection from leads and pressure ridges, or as creep due to the flexure of the ice sheet [49].

Researchers are interested in how waves propagate in icefields, how they scatter and attenuate, how the waves affect the floe size distribution, how they contribute to the dynamics of the ice margin due to collisions, and the relationship between the sea state, ice conditions and noise spectrum [49]. Wave decay observations in MIZ regions have previously been conducted using shipborne wave recorders, upward sonar from submarines, and airborne laser profilometry [49]. The use of a directional wave recording buoy has been commonly used in open and diffuse water, or an assortment of accelerometers, tiltmeters and strainmeters on ice floes to perform the same function as the directional wave buoy for wave observations [49]. From reviewing these observations, Wadhams [49] concludes that the attenuation of waves with respect to the distance into the pack has a negative exponential relationship, with the attenuation coefficient decreasing as the wave period increases over most of the spectral range. The directional spectrum inside the icefield becomes isotropic within a few kilometers of the ice edge. Lastly, some wave energy (a small percentage) is reflected from the outer icefield edge even when the edge is compact [49].

2.3 Sea Ice Formation, Growth, Deformation and Melt

2.3.1 Sea Ice Characteristics

Sea ice comprises of pure ice, brine, salt inclusions and air, and shows significant heterogeneity due to its microstructure being determined by the way in which the ice forms or melts, the ice profile's salinity and temperature history, the interaction of chemical, biological and physical processes, and the number and distribution of channels of brine drainage [23, 28]. Under

standard temperature and pressure conditions found on the Earth's surface, the crystallography of ice takes on a form called "ice I" [49]. This structure resembles a beehive-like configuration with slightly skewed hexagons, which causes the ice to have anisotropic physical and mechanical properties, see Fig. 2.2 [49].

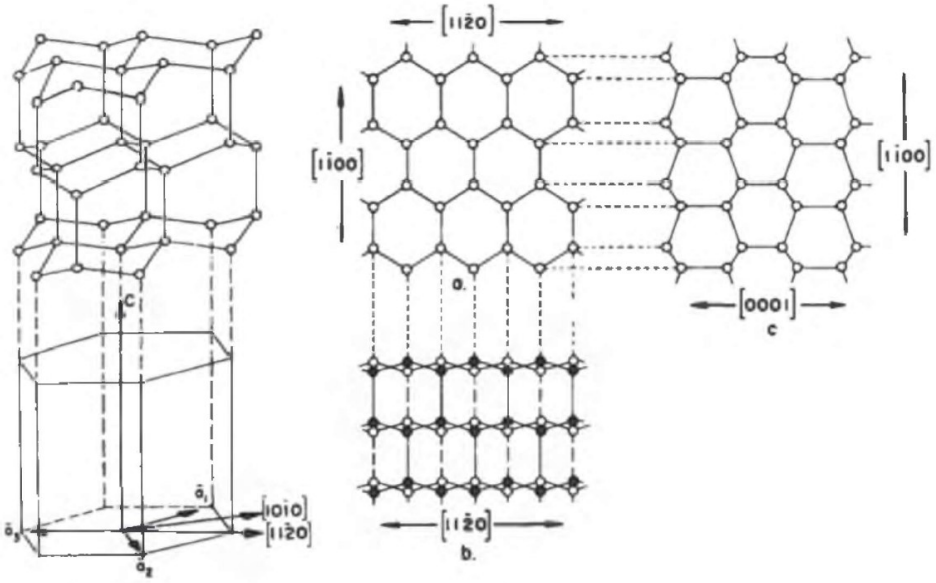

Figure 2.2: Diagram showing the crystal structure of ice I and the a-, b-, and c-axes, reproduced from Wadhams [49].

In calm water conditions, sea ice crystals form on the surface of the ocean in the form of small discs (2 mm to 3 mm in diameter) [49]. The discs grow laterally (in the a- and b- axis directions, which are orthogonal to the c-axis) until the disc shape becomes unstable, and the crystals take on a hexagonal, stellar shape, with dendritic arms [49]. The fragile dendritic arms break off and a mixture of discs and arm fragments is formed, with any turbulence causing further break up leading to small randomly-shaped crystals which increases the density in the surface water. This ice type is known as frazil or grease ice [29, 49]. In calm conditions, the frazil ice crystals freeze together, forming a thin continuous sheet of young ice [49]. After ice sheets have formed, a different growth process occurs, where water molecules freeze to the underside of the existing sheets - this process is called congelation growth and yields first-year ice [49]. In the Antarctic, a single season of first year ice reaches a thickness of 0.5 m to 1 m [49].

In turbulent water conditions, as is at the extreme ice edge, the high energy Southern Ocean wave field maintains the dense grease ice [28, 49]. The grease ice experiences cyclic compression, during which crystals may freeze together forming small pieces of coherent slush which grows by accretion from surrounding grease ice and becomes more solid via continued freezing between crystals [49]. This ice is known as pancake ice due to the raised edges of the ice circumference caused by grease ice deposits [49]. At the edge of the MIZ, pancakes are a few centimeters in diameter and grow in both thickness and diameter the deeper into the MIZ they

are situated with a diameter up to 3 m to 5 m and thickness up to 50 cm to 70 cm [49]. The surrounding grease ice continues to grow and add to the pancake ice growth due to the ocean surface not being completely insulated by ice and therefore latent heat can be removed by the large ocean-atmosphere heat-flux [49]. Even further into the MIZ (approximately 270 km from the ice edge), pancakes start to freeze together using the grease ice as a binder, forming large ice floes and then a continuous sheet of first year ice called consolidated pancake ice [29, 49].

When sea ice grows, salt is not able to enter the crystal structure due to the gaps within the structure being too small for the ions to fit into [28, 49]. Brine that is rejected from growing ice sheets is accumulated in the spaces between rows of dendrites, thus trapping brine within the ice [49]. In a similar manner, air bubbles are also trapped within the growing ice sheet, giving the ice a matt, white appearance and it is responsible for the variable density of sea ice samples [49]. As ice sheets age, the brine concentration decreases due to a network of brine drainage channels created over time [49]. The strength properties of sea ice are dependent on brine volume, thus brine drainage provides greater strength to ice during its second winter compared to its first [49].

Katabatic winds (wind caused from cold dense air flowing down a slope) blow snow off the top of ice shelves in coastal regions onto the sea ice [49]. Since the sea ice is so thin, in some cases the snow is sufficient to bring the ice surface below sea level causing infiltration of sea water into the snow on the surface [49]. This leads to the formation of a wet slushy layer on the ice surface, or the formation of a snow ice layer between the original surface and the unwetted snow [49]. The resulting flooded layer affects passive microwave signatures, making it difficult to identify multi-year ice, and it also impacts the mass and energy balances of sea ice which changes the modelling inputs needed for accurate representation [49].

After ice extent has reached its maximum, winter ice moves seaward, breaks up and begins to completely melt at the retreating ice edge [49]. The ice melts completely indicating that almost all Antarctic sea ice is first-year ice [49]. Only in the Ross Sea, Weddell Sea, and to a slight extent the Bellingshausen Sea, do significant amounts of pack ice survive, becoming multi-year ice [49]. Although melt pools hardly occur, Wadhams [49] observed extensive melt ponds on thick multi-year ice floes near the ice edge in the north-western Weddell Sea.

In the Antarctic MIZ, the sea ice properties are linked to the ice concentration and the specific ice types, such as consolidated pack ice, solitary pancake ice floes, and the fluid-like frazil/grease ice [28, 39]. The heterogeneous and dynamic composition of sea ice is also influenced by a combination of mechanical phenomena like floe collisions, form drag between the grease ice and pancake ice, and skin drag [39].

Paul et al. [29] investigated the properties of frazil ice, including its rheological properties which are essential for numerical simulations of sea ice dynamics. The researchers of the study sampled the frazil ice of the Antarctic MIZ and measured the viscosity. The collected data enabled the calculation of shear stress and shear rate of each sample. The maximum viscosity found was 275 Pa s [29].

Skatulla et al. [39] studied first-year ice samples of the Antarctic MIZ from solitary pancake ice floes in order to obtain its physical and mechanical properties. The uniaxial compressive strength for pancake ice was found to be approximately 2.3 MPa, and the bulk and shear moduli in the longitudinal direction were approximately 3.7 GPa and 1.3 GPa, respectively [39].

2.3.2 Sea Ice Thermodynamics

Thermal properties of sea ice include thermal conductivity, latent heat of fusion, specific heat, and extinction coefficient for radiation, all of which determine the rates of sea ice growth, decay, and phase transitions during melting and freezing [49]. Wadhams (2000) states the importance of obtaining these properties for both sea ice and snow because snow cover influences the thickness to which sea ice can grow due to its low thermal conductivity which reduces heat loss from the surface of the sea ice [49]. Heat conduction through sea ice is influenced by the ice porosity, solid salt content, and liquid brine which has the most complex effect [49]. The brine is a concentrated solution contained in small cells in the ice and acts as a thermal reservoir which retards heating or cooling of the ice. Therefore, specific heat of the sea ice is a function of temperature and salinity where an increase in temperature or salinity increases the specific heat since the brine volume becomes large near the melting point [49].

Typical sea ice thermal conductivity near melting point is substantially reduced in comparison to that of pure ice due to sea ice containing brine and air which are 25% and less than 1% of pure ice conductivity, respectively [49]. The temperature and salinity affect the specific heat of sea ice mainly near the melting point and become insignificant below $-8\,^{\circ}\mathrm{C}$ [49]. With regards to solar radiation, the rate of absorption depends on the material properties, radiation incidence angle and wavelength. The decay of energy penetrating vertically into the snow or ice cover is exponential (for any wavelength) and can be represented in terms of a spectral extinction coefficient [49]. This coefficient varies significantly amongst the ice types, where radiation is extinguished much quicker in snow than in sea ice and the extinction rate is lower with shorter wavelengths compared with longer wavelengths [49]. Albedo refers to the fraction of incident solar radiation on ice or snow cover that is immediately reflected [49]. An area-averaged bulk albedo is a common quantity used in models which is highly variable and difficult to define in summer when the surface is a mixture of melt pools, bare ice, snow-covered ice and melting ice [49]. The variability is one of the bigger problems of ice thermodynamics in terms of modelling [49].

2.3.3 Sea Ice Dynamics

Several factors influence sea-ice dynamics such as ocean and atmospheric circulation, ocean properties and ventilation, sea ice interaction with ice sheets and coastal configurations, fresh water input due to melting ice, and sea ice distribution and concentration [20, 23]. The

spatial and temporal evolution of sea ice and wave attenuation are influenced by the frazil ice damping effects and complex ice floe collision dynamics [29]. Globally, the annual sea ice advance and retreat represents one of the biggest albedo and physical changes on the Earth [20, 23]. The morphology of ice cover is influenced by movement caused by winds and currents. As a result of the stresses due to winds and currents, coastal polynyas, leads and pressure ridges form [49]. Thermodynamics and dynamics of sea ice allow for small- and meso-scale ice-ocean models to be constructed which may describe specific aspects of ice cover. The results of these models may then contribute to GCMs of the atmosphere and ocean which will yield global atmosphere-ocean system behaviour and potentially predict the the role of sea ice in climate variability and change [49].

There are four components of sea ice dynamics that make up the air-ice-ocean system, namely, momentum balance, ice strength, ice rheology, and mass balance. Momentum balance corresponds to the type and magnitude of forces acting on each element of the ice cover; ice strength refers to the type and magnitude of stress required to fracture the ice causing it to become discontinuous; ice rheology describes the behaviour of the ice cover as a specific material reacting to various stresses; mass balance corresponds to the ice thickness characteristics and its dependence on growth, melt and ice drift and deformation [49].

To derive the momentum balance, all the forces acting on the sea ice must be considered using Newton's Third Law of Motion. It expresses the force balance for an element as the product of an element's mass and acceleration is equal to the sum of the air stress, water stress, Coriolis force, internal ice stress, and force due to sea surface tilt [49]. Wind forcing contributes significantly to air stresses as well as turbulence underneath the sea ice [20, 40, 49]. The constant of proportionality that links wind speed to the stress exerted on the ice surface is the drag coefficient, and is a function of surface roughness. The wind speed is defined at an arbitrary distance above the ice (the anemometer height) since the frictional drag on the surface leads to a reduction of wind speed and a change in direction closer to the surface of the ice [49]. Two kinds of surface roughness are found in sea ice, a small-scale roughness at the top of the surface of undeformed ice floes, and larger-scale roughness of pressure ridges and rafted ice floes with protruding edges. The drag coefficient is thus split into skin friction drag which is due to the surface of the undeformed ice, and form drag which is due to larger obstructions of individual ice structures to airflow [49].

In the same way that air stresses act on the top surface of the ice, water stresses occur on the bottom surface of the ice. In this case, the force is due to the relative motion of the water and the ice. This force is either preventing movement of the ice floe due to wind forcing or trying to accelerate the ice floe due to strong currents [49]. The water-ice drag coefficient is a function of the bottom surface roughness and also varies with the type of ice, ridging density, and frequency of leads or floe edges causing obstructions to flow. The drag can again be split into skin friction drag and form drag but it is not commonly done with water stresses [49]. The difference between smooth ice and ridged ice for water drag is significantly greater relative to the air drag differences. This is due to the oceanic boundary layer under the ice being

30 m thick whereas the atmospheric boundary layer is approximately 1000 m thick, thus for an obstruction of the same height above and below the ice, the water drag coefficient would be influenced more than the air drag coefficient since the obstruction takes up a larger fraction of the oceanic boundary layer in comparison to the fraction taken up by the atmospheric boundary layer [49]. The water drag coefficient is also affected by melting and freezing which influences the whole form of the boundary layer under the ice. Melting reduces the drag by increasing the density stratification near the surface which changes the vertical momentum transfer. Freezing thus increases drag by decreasing the stratification [49].

On a geophysical scale, Coriolis force becomes important and influences sea ice motion, ocean currents and global winds [49]. It depends on the ice mass, the Earth's angular velocity, the velocity of the ice and the latitude degree of the ice. The force direction is 90° left of the direction of the ice velocity in the southern hemisphere. The Coriolis force at the equator is zero and is maximum at the poles, therefore it is an important factor in ice dynamics especially for larger ice types such as icebergs [49].

Stresses transmitted through ice can be due to winds or currents, and are difficult to measure and parameterise in models. Sea ice is not a rigid material and has a thickness interaction in its response, for example, it can open up which forms leads or crushed which forms ridges. Therefore, the ice internal stress is a function of its rheology, strength and thickness distribution [23, 49].

The wind on the top surface of the ice drives the sea ice which causes the water on the bottom surface of the ice to be driven due to the water frictional drag. The motion of the water diminishes the deeper into water it goes. The pattern of the changing speed and direction in the top surface wind and bottom surface current due to the wind-generated motion in the open sea and Coriolis force is called the Ekman spiral [49]. Ice drifts in the direction of geostrophic wind, and since this wind blows parallel to the isobars, the empirical Zubov Law (1945) states that ice drifts parallel to the isobars [49]. The Nansen-Ekman ice drift law stated that ice moves at 2% of the wind speed and in a direction which is approximately 30° right of the surface wind direction in the Northern Hemisphere [49]. Both the Zubov law and Nansen-Ekman law are rules of thumb which prescibe general behaviour of ice, and in the Antarctic, conditions may be different due to much shallower pressure ridge keels [49]. Wind is the main driver of sea ice variability in the Antarctic, promoting expansion by advection of sea ice northward, and cooling and freezing [20], with warmer onshore winds possibly causing ice edge retreat [20]. According to Maksym [20], wind forcing is a factor that may explain trends in all areas of the Antarctic with the exception of regions in the WAP where warming is a significant factor contributing to the trends. Models suggest that ice in the Ross Sea and inner Weddel Sea has thickened and ice in the Bellingshausen Sea has thinned [20]. Atmospheric circulation and drift tend to push the ice closer to the thickening regions which shows that the above trend in ice thickness is mainly dynamically driven by wind and deformation [20].

2.3.4 The Importance of Understanding Sea Ice Dynamics in the Marginal Ice Zone

Massom and Stammerjohn [23] note that it is important to understand the formation, growth and melt processes when considering sea ice change and variability. This is because the sea ice distribution and growth are governed by complex relationships between dynamics and thermodynamics [23]. The recent increase in overall Antarctic sea ice extent is related to the springtime stratospheric ozone depletion. Massom and Stammerjohn (2010) suggest that, as ozone levels recover, significant sea ice reduction will be observed in the future [23]. On the other hand, Polvani et al. (2013) suggests that the positive trend in sea ice extent in Antarctica is mainly due to large internal variability of sea ice systems and not due to anthropogenic forcings [30]. Variation in wind is associated with two main modes of climate variability, namely, the SAM and the ENSO, where strongest variability is seen when a negative SAM is coupled with a warm El Niño or a positive SAM with a cool La Niña [20]. The ozone hole has played a role in strengthening the SAM, which cools most of the coastal Antarctic region [20]. It was suggested that this would contribute to deepening the Amundsen Sea Low (ASL) which would drive an increase in sea ice [20]. This response is modulated by ocean processes, but in the short term, the effects of anthropogenic forcing may be counteracted by effects ozone depletion [20].

Understanding atmospheric forcing and sea ice dynamics is necessary because observed sea ice data cannot be fully explained by only using references to major climate variability modes [20, 40]. The rate of mixing of the ocean surface contributes to the rate of mass, heat, and energy exchange between the ocean and atmosphere [40]. Sea ice reduces this rate of mixing yet the current prediction methods do not describe the range of conditions that occur well enough [40]. Sea ice also plays a role in regulating the biological pump, the uptake and sequestration of CO_2 from the atmosphere, ocean upwelling and outgassing, and ocean acidification of the Southern Ocean - all which is still poorly understood according to Massom and Stammerjohn (2010) [23]. Therefore, it is imperative to understand the natural variability of Antarctic sea ice when improving models and their respective predictions [20].

2.4 Sea Ice Dynamics Models

There is now four decades worth of observations of Arctic and Antarctic ice cover, but it is evident from models that this time frame may be too short to conclude a forced trend in Antarctic sea ice [20, 21, 30]. Before the satellite records, Antarctic observations were slim, and data prior to the 1960s includes the use of whaling records and glacial ice cores to determine sea ice extent [20].

Metrikin et al. [24] classifies modelling approaches into three main groups, namely, empirical and statistical modelling, experimental data series methods, and physics based modelling.

Empirical and statistical models are based on observed data and analyses of experimental data, with a main advantage being its numerical efficiency, but a major drawback is the oversimplification of complex systems and processes which may yield unrealistic results. Experimental data series methods use the data, which is recorded in full-scale trials or model tests, as inputs to numerical simulators. The advantage of this approach is that it allows for a system to be custom-modelled for a specific set of conditions, although a disadvantage is that it is difficult to modify the model to fit various other cases with different boundary conditions. Furthermore, the results from the model are only valid if the simulated and recorded data are in good correspondence. Physically based models use the governing laws of physics as its foundation and are able to provide much more comprehensive descriptions of of processes and interactions, thus it is able to reproduce real scenarios with a certain degree of accuracy. Consequently, these models contain large computational complexity, and in some cases, it can prohibit real-time applications [24].

Large scale models are typically measured on scales larger than $10\,\mathrm{km}^2$ with sea ice described using a continuum approach [32]. In contrast, small scale models consider $10\,\mathrm{km}^2$ scales or less and usually have lower sea ice concentrations, thus the discontinuous nature cannot be ignored [32].

Current AOGCMs have sea ice components which are usually used to predict ice thickness/volume, fractional ice cover, snow depth, surface temperatures and horizontal velocity. The sea ice albedo is also typically prescribed based on ice thickness, snow cover and melt pool effects [33]. The complexity of the sea ice dynamics component in current AOGCMs varies from simple models of cavitating fluid to more advanced viscous-plastic models [10, 33]. Hunke and Dukowicz (1997) introduced the elastic-viscous-plastic model which is starting to be implemented more often in climate models due to its efficiency especially in parallel computing [13, 33].

Sea ice thermodynamic components have shown slower progression, and they typically consist of constant conductivity and heat capacities for the snow and ice, a heat reservoir simulating the effect of brine channels in the ice, and various layers with the uppermost layer representing the snow [33]. Some more sophisticated thermodynamic models introduce salinity-dependent conductivity and heat capacities; some even include snow ice formation which often happens in the Antarctic sea ice system when ice floes are submerged by the weight of the snow above it causing freezing of the flooded snow layer to the ice floe surface [33].

Instead of modelling ice as a uniform slab, many sea ice models use a sub-grid scale thickness distribution with a range of thickness categories. This ensures a more accurate simulation of ice growth and melt rates which significantly influences ice-ocean albedo feedback processes. It also aids in more physical ice ridging formulations and rafting events based on energy principles. Advanced ice floe ridging parametrisation has been lacking in sea ice dynamics models, although ridging mechanics and its relationship between ice thickness distribution have improved [33].

Rabatel, Labbé, and Weiss [32] modelled the dynamics of an assembly of rigid-body ice floes with random shapes and size which incorporated skin drag due to the atmosphere and ocean. The granular model is based on an event-driven algorithm instead of a molecular dynamics scheme. It makes use of simplified momentum equations for the motion of the floes and resolves linear complementarity problems for the floe-floe collisions. The loss of kinetic energy due to contact is described using a constant coefficient of restitution and coefficient of friction [32]. The model describes the dynamics of a large number of ice floes within a reasonable processing time. It does not account for energy dissipation due to vibrations and waves, but it describes elastic collision behaviour of floes [32].

Alberello et al. [1] developed a Lagrangian free drift model which shows the movement of individual pancake ice floes in the Antarctic MIZ over the time frame of days. The Arctic Ice Dynamics Joint Experiment (AIDJEX) model was used, which incorporates the external stresses due to wind, ocean currents, Coriolis and ocean tilt, into the momentum equation [1]. A comparison between the model and in-situ measurements of buoys on pancake floes showed that pancake ice floes are extremely mobile and its drift velocity correlates well with the wind velocity. It was found that the wind is the dominant forcing and no correlation was found with wave-in-ice activity [1]. The study highlights the need for better understanding and modelling of the drag coefficients and ice thickness and the temporal and spatial variation.

Hunke and Zhang [12] compare the use of VP and EVP models in simulating realistic, high resolution Arctic sea ice dynamics. The motion fields of the models are also compared to that of drifting buoys in the Arctic [12]. The models are based on a dynamic-thermodynamic sea ice model with identical domains, boundary conditions, initial inputs and forcing fields. The VP model's dynamics component uses a semi-implicit algorithm by Zhang and Hibler (1997), except a Jacobi iteration is used to replace their over-relaxation technique, which allows for the VP code to be vectorised and reduces the computational time [12, 51]. Both the VP and EVP models adopt the advection scheme of Hibler (1979) [10, 12]. A two-dimensional momentum equation is used to describe the force balance per unit area of the ice pack, which includes external forcing on the ice due to wind, ocean stresses, sea surface slope, and Coriolis forces [12]. An internal stress tensor is used to represent the strength of the ice. The models are based on a viscoplastic rheology which was proposed by Hibler (1979) [10]. This is given by a constitutive law which relates the internal stress of the ice to the strain rate via an internal ice pressure and nonlinear shear and bulk viscosities such that the principal stress components lie on an elliptical yield stress curve with a major-to-minor-axis-ratio of 2 [10, 12]. Hibler (1979) prescribed upper bounds based on ice thickness and concentration for the viscosities in order to regularise the behaviour, such that when the ice pack is rigid, it is treated as a linear viscous fluid with very slow creep. A lower bound is also prescribed for the viscosities [10, 12]. The time step restriction for explicit discretization of VP equations is directly proportional to the square of the mesh size and inversely proportional to the bulk viscosity thus making it necessary to use implicit methods for time steps larger than a few seconds in areas where ice is close to being rigid. In summary, the VP ice rheology consists of a viscoplastic constitutive law, equations for viscosities, strain rates, and linear viscous

regularisation for extreme values of viscosity [10, 12].

The EVP model has an improved transient response of the solution compared to the VP model leading to a more accurate description of sea ice behaviour [12, 13]. According to Hunke and Zhang [12], the main purpose of developing the EVP model was to improve on the numerical efficiency of the VP model. The EVP model was 30% faster than the Jacobi VP model with regards to the total CPU time required. Furthermore, it performs substantially better on multiprocessor machines due to the EVP model being explicitly discretised [12].

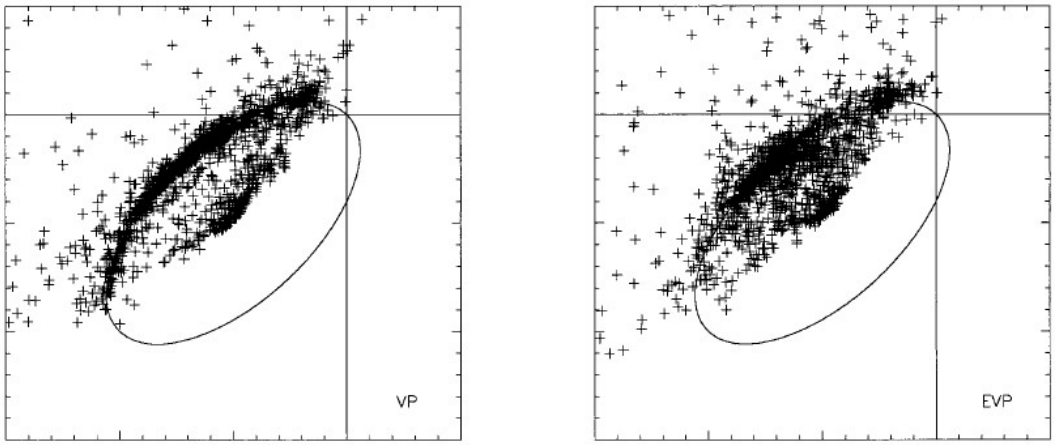

Figure 2.3: Plots showing the comparison of the VP model and EVP model principle stress components on the yield stress curve, reproduced from Hunke and Zhang [12], where the crosses represent samples of the principal stress components.

Both models found large strain rates near the ice edge due to low ice strength associated with either smaller ice thicknesses or lower ice compactness, along with the viscosities being at a minimum and ice in this region behaving in a linear viscous manner [12]. The central pack ice is compact, and the elastic contribution to the models is quite small in the central Arctic and very small divergence occurs in both models. The VP model is using maximal viscosities with a linear viscous regime, and the EVP model has elastic waves active for this region of the Arctic. However, the velocity magnitudes are so small that differences between the model simulations are insignificant [12]. The regularisation of the constitutive law in the VP model causes the principle stress components to stray from the elliptical yield curve, especially in fairly rigid regions which tend to fall inside the ellipse area, as seen in Figure 2.3 [12]. The EVP model also causes deviation from the plastic behaviour due to the introduction of elasticity in the visco-plastic ice properties. These effects are especially seen at extreme viscosities [12]. In terms of sea ice distributions, the VP and EVP models produce very similar results, with slight differences in areas with concentrations above 90%. The differences between the thickness distributions of the models are also small and generally less that 0.5 m. The models show the largest differences in the summer season, with the thickness and concentration differences being 13% and 7% respectively [12]. The models' transient responses, such as their response to imposed surface forcing, are where large differences lie. The VP model is significantly slower in response to changes in winds which present as lower

ice speeds and different vector directions compared to the EVP model. This is due to the error associated with numerical discretisation, where it is most significant in areas with ice concentrations above 80% and notably worse above 90% [12]. Overall, both ice dynamics models produce equivalent sea ice behaviour in timescales that are larger than a week. Thus, climate simulations using either model are comparable, although the EVP ice dynamics model significantly improves computational efficiency [12].

Kohout, Meylan, and Plew [16] introduces a wave attenuation model for the MIZ by means of a scatter model and a combined scatter and drag model. It was found that the addition of drag to the scatter model improves the rate of decay of the wave attenuation coefficient. The study notes that the choice of a constant drag coefficient was an oversimplification for the model as drag would vary with ice concentration and distance into the ice field [16]. Furthermore, neither scatter nor drag models accounted for the dampening at long periods or rollover at short periods. The study concluded that parameterisation of more physical processes is required to accurately model the wave attenuation specific to the MIZ [16].

Marquart et al. [22] introduces a novel CFD framework for small-scale wave-ice interaction dynamics, focusing on pancake and grease ice rheology in the Antarctic MIZ. The model involves free-floating ice floes in interstitial grease ice, where the floes experience elastic collision dynamics, and the system is subjected to ocean wave action. The sea ice dynamics model is based on the momentum balance governing equation. The Cauchy stress tensor represents internal ice reaction forces, and in-plane stress caused by the waves is derived from the linear wave theory. The external forcing is made up of two components: the viscous component represents the skin drag on the entire ice-ocean interface, and the Froude-Krylov force from the wave-induced pressure field imposed on an ice floe circumference [22].

The proposed model represents the sea ice rheology as two separate constituents, grease and pancake ice, with their own material characteristics. The grease ice is represented as a fluid-like viscous-plastic material. The pancake ice floes are modelled as a solid-like material with small deformations described using generalised Hooke's Law [22]. The small-scale modelling is justified by using an inner sampling domain which is smaller than the actual simulation domain, thus producing spatial and temporal fluctuations of strain rate distribution based on the ratio of pancake floe diameter to wavelength which is unaffected by the simulation boundary [22]. The study used three realistic sea ice layouts and one idealised configuration, shown in Figure 2.4. The most homogeneous layout was chosen to compare against the ideal sea ice layout in order to study the error introduced when the ice floe shape and diameter are disregarded [22]. The study found that the dynamic sea ice response, in homogeneous conditions, becomes independent of the details of the floe distribution for waves with periods larger than 16 seconds. This was expected as the larger waves become less likely to interact directly with single ice floes thus the detail of the distribution becomes less significant [22]. For smaller wave periods, the error between stress and strain rate curves increased, indicating that the actual floe geometry is significant in the mechanical sea ice behaviour [22].

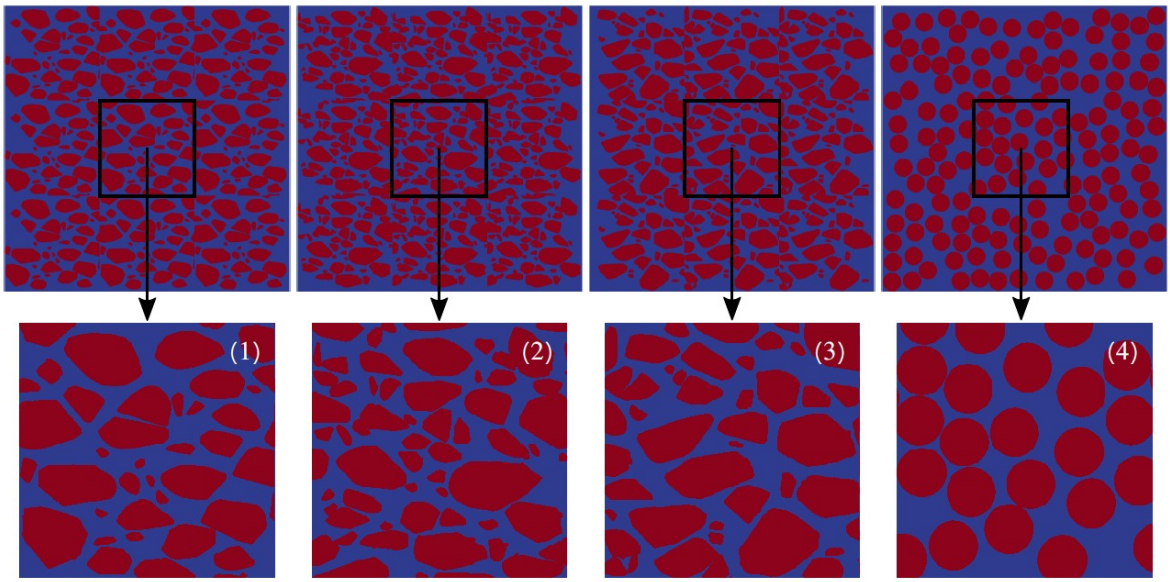

Figure 2.4: Snapshots showing the four different sea ice cases modelled and investigated by Marquart et al. [22], where the red objects represent pancake ice floes and the blue surrounding it represents the grease ice. Layouts 1-3 represent three different realistic layouts and layout 4 is an idealised configuration.

Wadhams [49] also reviewed various sea ice models, starting with the AIDJEX project from 1970 to 1977. The project produced data sets on ice dynamics, thermodynamics and deformation, with the aim of developing a sea ice model to make predictions on small time scales of one day and spatial scales of 100 km [49]. The model used a plastic rheology which required a Lagrangian grid to trace strain state of an ice parcel. Retaining this information was complex numerically and computationally expensive [49].

Another model, by Hibler III [10], has become the common approach for sea ice modelling and uses the viscous-plastic rheology. This method overcomes the computational issues of the AIDJEX model because it uses an Eulerian grid instead of a Lagrangian grid [10, 49]. The model has prescribed wind forcing, incoming radiative fluxes and thermal ocean flux. At the same time, a model by Parkinson and Washington [27] came about and was applied to both hemispheres. The model dynamics were in free drift which produced realistic results for Antarctica but unrealistic results for the Arctic. The model predicted the greatest ice thickness to occur in the centre, whereas the Hibler model showed a build-up of thickness around the Arctic coastlines due to ridging [27, 49].

During the 1980s, model development focused on improving the parametrisation of the coupling between ice and the ocean and atmosphere, and using better forcing data. Alternative rheologies were explored, especially with the large new data on MIZ dynamics from the MIZEX project. Some researchers developed rheologies which involved interactions between individual ice floes which produced a yield curve based on statistics, whereas other researchers developed a cavitating fluid model with no associated shear strength and the ice is free to drift but

has a corrective ice velocity for convergence [49]. The following major development was a basin-scale coupled ice-ocean model. The coupled model allows for a joint response of the ocean and ice to be produced which provides better predictions of the ice edge position [49].

Wadhams [49] summarises the recent directions of model developments into six main points. Firstly, incorporating ice-ocean models into GCMs will allow the role of sea ice dynamics and thermodynamics in climate change to be assessed. Secondly, developing regional sea ice models allows for better study of the MIZs, shelf seas or convection regions. Assessing the response of sea ice to varying key parameters, such as, snow, air temperature, river runoff, albedo changes, or ocean heat flux, will allow for sensitivity studies to be carried out. The fourth focus is on new formulations of key processes in sea ice dynamics and thermodynamics, for example, ice ridging. The penultimate point is the use of more powerful computing to reduce the grid size of models down to a few km, in order to obtain more precise data. Lastly, developing operational models in order to provide short-term forecasts [49].

Marquart et al. [22] comments that most modern dynamic and thermodynamic models used in global climate predictions are large-scale models in the order of 100 kilometers. These models use a viscous-plastic rheology to relate internal stresses of the sea ice to the strain rate. Thus, such models adopt a blurred/continuous approach where heterogeneous ice characteristics are modelled as a single large homogeneous material which has averaged properties, and where ice-ocean interactions have been parameterised [22, 32]. The model dynamics is based on a momentum balance, with two continuity equations that inform the ice thickness and concentration which accounts for the growth and deformation effects. Marquart et al. (2021) explain that sea ice deformation cannot be solely described by a viscous-plastic rheology because as the sea ice drift on a scale less than 10 kilometers has reduced accuracy and fails to reproduce sea ice deformation at even smaller scales [22]. Furthermore, the VP model by Hunke and Dukowicz (1997) has a large linearisation error in its time discretisation thus weakening or delaying its transient response to conditions which are changing rapidly [12, 13].

On a larger scale, sea ice characteristics strongly affect the magnitude and spatial distribution of changes to the high-latitude climate yet, evaluating the sea ice component of models is challenging due to insufficient observations of key variables, for example, the lack of ice thickness data [33]. Even when it is possible to quantify the errors in the sea ice models, it is difficult to isolate the causes of these errors. They might be from deficiencies in the representation of the sea ice or from erroneous simulation of the atmospheric and oceanic fields which drive the ice movement [33]. Most AOGCMs underestimate the southward heat transport from the equator in the tropical and subtropical zones of the Southern Hemisphere [33]. In terms of wind stresses, almost all of the model simulations produce a Southern Hemisphere wind stress maximum that is higher than the reanalysis estimate. The errors in the Southern Ocean wind stress in the the control integrations can adversely affect the simulation and potentially the oceanic heat uptake due to climate change [33]. Moreover, many models also have a "too-warm" bias in the sea surface temperatures of the Southern Ocean [33]. The Southern Ocean simulations have a large wind stress error, as mentioned above, and

this partly affects the simulated location of the Antarctic Circumpolar Current (ACC), which is too far north. Due to the Antarctic Intermediate Water (AAIW) forming on the north side of the ACC, the AAIW mass water properties are also distorted, and are typically too salty and too warm [33]. The poor Southern Ocean simulations influence the transient climate response to the increase in greenhouse gases due to the result of the oceanic heat uptake, and such errors will also largely impact the reliability of the projections of sea level rises [33].

More specific to sea ice models, of the fifteen AOGCMs evaluated by Randall et al. [33], the mean annual cycle of ice extent is exaggerated in the Southern Hemisphere, with too much sea ice produced in September and too little produced in March. Even with an approximately correct areal extent, the regional distribution in many of the models is poorly simulated [33]. The multi-model standard deviation from the model mean sea ice extent is generally narrower in the Northern Hemisphere than in the Southern Hemisphere [2, 33]. Even in the best case, the range of sea ice extents simulated exceeds 50% of the mean, suggesting that the sea ice projections are still quite uncertain [33].

There are huge numerical costs of accounting for the heterogeneity and floe-floe collisions, as well as challenges with coupling the small-scale models with larger-scale atmosphere and ocean continuous models. This has resulted in sea ice models being less developed than large scale models [32].

Another area of neglect is fast ice. The resolution of most GCMs are too coarse to account for the relatively narrow band of fast ice that borders the Antarctic coastline [23]. It has been shown that fast ice in the Antarctic is a good indicator of climate change, however no model predictions of the fast ice have been made in response to IPCC (2007) climate change scenarios [23, 41]. Furthermore, sea ice cover is treated as a continuum in GCMs and coupled sea ice models, thus these models also neglect ocean surface waves despite the significance that they hold [23].

In summary, current large-scale models do not accurately represent key features of Antarctic ice cover [20]. Large biases occur in modelling the ice extent, and the observed variability is smaller than the models' inter-annual variability results. Many models failed to reproduce the observed increase in Antarctic sea ice extent, and it suggests that models are unable to adequately simulate the processes that have driven the sea ice extent and variability over the previous four decades [20]. Studies have, however, been able to show that the observed trends fall within the range of the models' natural variability [20].

2.5 Fluid Structure Interaction

FSI is the interaction between movable or deformable structures and a surrounding or internal fluid flow; it is the overlap of fluid dynamics and solid mechanics [38]. There are two types of mathematical approaches used in solving computational dynamics, Eulerian and Lagrangian

methods. The dynamics of a system in the Eulerian method are taken as measurements of the evolution of the system with respect to a fixed coordinate system (the spatial frame) [38]. Physical equations are naturally formulated in the Eulerian method because the field variables, especially in fluid physics, are expressed as functions of fixed coordinates. On the other hand, solid mechanics equations are written with respect to individual material cells which deform or displace relative to the objects movement, thus a Lagrangian coordinate system (material frame) is better suited [38]. The Lagrangian method allows for easier access to results at points within the moving or deforming objects [38]. In typical computational continuum mechanics, solids are simulated using Lagrangian frameworks such as finite element methods with moving nodes, whereas fluids are simulated using Eulerian techniques such as finite difference or finite volume methods which have fixed spatial grids [15]. The decision is commonly based on the computation of stress, where solid stress uses total deformation due to the relative positions of the material nodes, and fluid stress uses the deformation rate from the velocity field through a fixed grid [15]. Moreover, fluid flow generally has larger deformations with mixing and inflow/outflow boundary conditions whereas solids generally have smaller strains and boundary conditions that move with the deformation of the shape. Combining the two methods to produce a fluid-solid simulation creates many issues due to the inherent differences between the Lagrangian and Eulerian frameworks [15].

FSI problems are generally too complex to solve analytically, thus they are analysed via experiments or numerical simulations. These problems can be solved using a monolithic or partitioned method, refer to Figure 2.5 for the various FSI schemes. The monolithic approach solves a large single system of equations for all the fluid's and structure's unknowns, simultaneously [38]. The partitioned approach has separate solvers for the fluid and structure, and employs a coupling method between the two components [38].

A partitioned approach is popular as it has a simple and modular implementation where it solves the fluid problem and structure problem separately with the interface values outputted back and forth from one solver to the other. The individual component solutions may be loosely or strongly coupled [38]. Dirichlet-Neumann (DN) schemes use standard partitioned approaches where the fluid problem is solved using a Dirichlet boundary condition (the structure velocity) at the fluid-structure interface, while the structure problem is solved using the Neumann boundary condition (the fluid stress) at the fluid-structure interface [38]. Loosely-coupled DN schemes are only stable if the structure density is much larger than the fluid density, otherwise numerical instabilities, known as the added mass effect, are introduced due to the energy of the discrete problem not accurately approximating the energy of the continuous problem [38]. To solve this issue, strongly coupled partitioned schemes can be used which sub-iterate between fluid and structure sub-problems during each time step until the energy at the interface is balanced. This scheme may lead to slow convergence issues, but this may be avoided by using Aitkens dynamic relaxation or reduced order models [38].

The Arbitrary Lagrangian-Eulerian (ALE) method is used in monolithic or partitioned FSI to consider the moving boundaries between Lagrangian and Eulerian frames by introducing

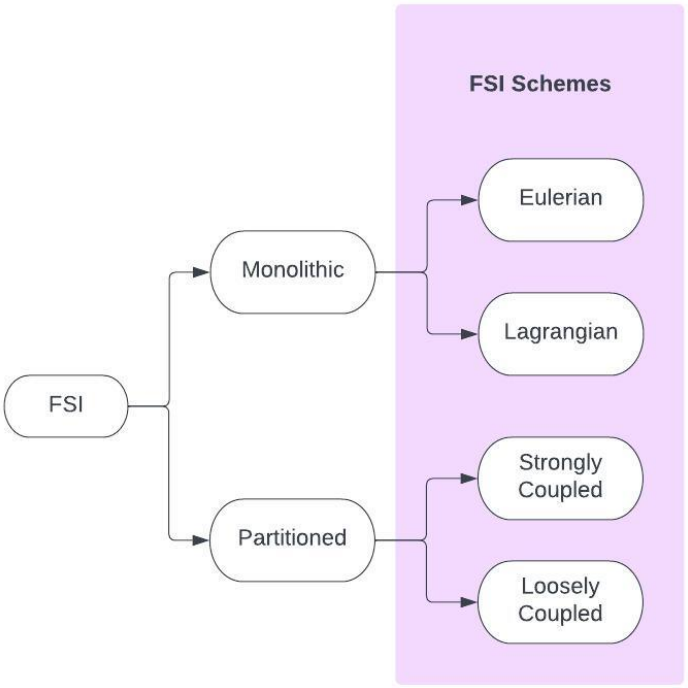

Figure 2.5: Breakdown of the different types of FSI schemes.

a third coordinate system (mesh frame) which matches neither spatial nor material frames. There is a mathematical mapping between the spatial frame and the mesh frame and another mapping between the material frame and the mesh frame, therefore at all times, the equations formulated in the material and spatial frames can be transformed to the mesh frame and then be solved [38]. A moving mesh or deformed geometry is created to allow for the apparent positions and deformations of the mesh elements to displace in the spatial frame. This is to show how the mechanical deformation changes the shape of the boundaries defined in an Eulerian domain [38]. The ALE scheme requires body-fitted meshes for all the structures, and calculation of grid velocities at each time step. This technique is known to be accurate and suitable for both compressible and incompressible fluids [38]. Alternatively, the immersed boundary method (IBM) or immersed finite element methods (I-FEM) treat moving boundaries without requiring a moving mesh and is therefore not sensitive to mesh quality [38]. In these methods, the fluid solver may be independent of the structural solver because the interactions are computed by interpolating the results in overlapping zones [38].

At the fluid-solid interface, kinematic and dynamic conditions must be satisfied. The kinematic conditions are such that the velocity and displacement at any point along the interface must be continuous across the interface (from fluid to solid or solid to fluid) [38]. Where a DN coupling scheme is implemented, the velocity and displacement are calculated at the solid side and then applied as boundary conditions to the fluid side of the interface [38].

To summarise the approaches, the monolithic approach requires code to be developed for

each particular combination of FSI problems whereas the partitioned technique preserves modularity in that separate exisiting solvers for fluids and structures may be used and then coupled together [38]. Furthermore, the partitioned approach may use more efficient techniques for solving the fluid and solid equations with different solvers which have been specifically developed to solve either solid or fluid equations. However, the development of accurate and stable coupling algorithms are required in partitioned schemes which adds further complexity as convergence is not guaranteed [38]. The typical FSI partitioned approach involves the interchange of surface forces, such as pressure, from the fluid and the displacement from structure, which is repeated until a convergence of flow and displacements are reached for each real-time step [38].

2.5.1 Previous Implementations of FSI

Timalsina, Hou, and Wang [45] show how FSI can be computed using the partitioned approach and combining the IBM with direct forcing. The study uses a non-conforming mesh method, known as the immersed boundary method, which uses a fixed grid, as opposed to a conforming mesh approach where the mesh updates at each time step due to movement or deformation of the structures [45]. The numerical method used solves the fluid problem with an additional forcing term which represents the effects of the structure acting on the fluid. The fluid equations are solved over the entire domain with a fixed Eulerian mesh, with the structure represented by a moving boundary which is tracked with a separate process [45]. There are, however, major limitations with IBM due to it primarily dealing with structures that do not occupy volume, and using rigid or nearly rigid structures results in highly stiff IBM systems which become difficult to solve numerically [45]. To overcome this, the direct-forcing method is used which implements the no-slip condition at the interface to the fluid momentum equations in order to directly compute the FSI force [45].

In the study, the fluid is modelled using the Navier-Stokes equations and the flow is assumed to be incompressible and viscous [45]. The structure is modelled using the linear elastic model [45]. The FSI forces are evaluated at the Lagrangian grid points, using a modified direct forcing technique, and then interpolated to the Eulerian grid [45]. The study looks at three different material types in two-dimensional simulations, namely, rigid, elastic solid, and thin-walled elastic structures [45]. The first case of a rigid cylinder is use to verify the method. The study found good agreement between the numerical measurements and that of published work [45]. The second case is of an elastic solid beam in a parallel flow of viscous fluid. The bottom end of the beam is fixed whereas the rest of the beam is free to move and deform. Initially the beam is at rest, and over time the beam starts to oscillate due to the fluid flow [45]. Thirdly, the study investigated flow past a hollow elastic beam. The beam is set up in the same way as the previous case, except it is now hollow and closed on all side such that no transfer of fluid can occur from the inside cavity to the outer fluid domain [45]. The study was able to accurately track the fluid-beam interaction and obtain the structure's movement and deformation [45].

With regards to sea ice, Wang et al. [50] employ a structured ALE method to analyse the motion response of ice floes in waves. They study uses the numerical wave-making method based on dynamic boundary conditions and linear wave theory[50]. It was found that the ice floes mainly move in an irregular pattern within the short-wave range whereas isolated floes engage in regular motion in the long-wave range. The researchers noted that further studies should be conducted to investigate the non-linear dynamics of floe collisions and break-up, especially taking into account the influence of fluid-structure interactions on the system [50].

Huang et al. [11] studies hydroelastic wave-ice interaction, with a FSI model that has the capability to predict overwash of the ice sheet. A partitioned multiphase FSI scheme was developed with the finite volume method in OpenFOAM. The case setup involves a numerical wave tank that generates a regular wave field in the fluid sub-domain and a thin ice sheet in the solid sub-domain which floats on the water surface [11]. The model was able to predict the wave transmission and reflection over a single floating ice sheet.

2.5.2 Reference Map Technique

The RMT is a relatively novel approach to FSI problems in a fully Eulerian frame without added approximations [15]. It is an explicit finite difference method for solids [15, 37]. The RMT computes the finite deformation of a solid in any dimension and is based on tracking where a material cell came from via a reference map field on an Eulerian grid [15, 37]. Both solid and fluid are discretised on the same fixed general grid which simplifies the coupling between the fluid and solid [37]. This technique can apply complex or non-linear material laws to objects undergoing large deformations.

Kamrin, Rycroft, and Nave [15] present two large-deformation static solid mechanics cases of in-plane strain, with each case having non-trivial, inhomogeneous deformation to robustly test the numerical method. The first case involves a circular washer which is fixed at its outer wall and a large-angle rotation is applied to its inner wall. The study uses the Levinson-Burgess hyperelasticity law for the washer since there is an analytical solution against which the results of the simulation can be compared [15]. The results of the numerical solution show striking agreement with the analytical solution, and equally high levels of agreement were found when the rotation angle of the inner wall was varied [15].

In the second static case, using the same hyperelasticity law as before, a circular disk is stretched into a triangular shape. There is no analytical solution for this case, and the case is used to show how the method can be used in scenarios where the reference and deformed boundaries differ [15]. The unstressed material perfectly formed into the equilateral triangular shape, with each point on the disk edge having moved radially outwardly to form the triangle edge [15].

Kamrin, Rycroft, and Nave [15] present three FSI examples of a hyperelastic solid coupled

to a weakly compressible, athermal fluid using RMT. The first case investigates the release of a pre-strained disk within a fluid. Both solid, and fluid are initially at rest, and as the simulation progresses, the disk produces several damped oscillations [15]. The continuous projection of the reference map at the structure boundary ensures that the shape of the disk is retained, and the numerical errors do not influence the shape over time [15]. The second simulation deals with an anchored rod with rounded ends within a fluid flow and investigates how the structure deforms in response to the flow around it. The simulation recorded 25 seconds of data, where the rod reached its maximum deflection at 10 seconds and then began to relax into a stationary configuration at 25 seconds [15]. Finally, the study investigated a flexible rotor, anchored at its centre, spinning in fluid. The rotor shape consists of two rods taken from the previous case. The rotor and fluid are initially at rest and the rotor is forced to move by imposing fluid velocities in specific directions (horizontally inward and vertically outward) [15]. Thus, the rotor is first pushed diagonally upwards and to the right, but over time the rotor starts to rotate about its fixed point [15]. The authors conclude that the finite-difference framework enabled the simulations to run relatively quickly compared to other FSI methods [15].

The RMT significantly simplifies the coupling between solid and fluid constituents in FSI applications by using the same fixed grid as the fluid phase for the finite-deformations in the solid [47]. The technique allows for the interaction of fluid and solid, and also solid and solid submerged bodies. It describes a blurred fluid-solid interface method using finite differences on a stand-alone Eulerian grid [47]. The level set method is used in tracking the fluid-solid interface. It is also used in the solid contact model as it naturally has a distance function which is used to produce a short-range separation force that acts once solids are close enough to each other [47].

Rycroft et al. [37] illustrate a number of FSI examples using an incompressible Navier-Stokes fluid interacting with neo-Hookean solids. The paper demonstrates the ability to simulate sharp corners of a solid object with a spinning flexible rotor which has seven sharp points [37]. The rotor is fixed on a pivot at its centre and both the solid and fluid are stationary initially. The pivot is given an oscillatory rotation applied to it via an external tether force. Over time, the disturbance to the fluid grows with multiple vortices forming throughout the domain. The robustness of the approach is tested using a flapping flag example, with a thin filament (modelled as a one-dimensional beam) clamped on its left end and submerged in rightward-flowing fluid [37]. This example is validated with experimental, analytical and numerical results from other papers. The method also shows an approach for solid actuation which allows one to apply time-dependent deformations to sub-regions of the solid [37].

The paper demonstrates multi-body contact with soft, deformable particles in a fluid-filled box [37]. The technique does not use moving meshes thus making it well suited for many solids coming into contact. Each solid is modelled with its own independent reference map. When two or more solids come close together, their extrapolated regions overlap and a weighted portion of the global stress is associated with each solid. A small contact stress is applied to

overlapping regions which prevents the solid interfaces from coming too close together. This avoids the possibility of solids sticking together from sharing the globally defined velocity field.

An advantage of using the RMT for FSI models is that it can handle solids that are both neutrally buoyant and those that are lighter than the surrounding fluid with no further modifications, as shown in Rycroft et al. [37].

The proposed research investigates the possibility of using FSI and RMT to create a sea ice dynamics model.

Chapter 3

Continuum Mechanics and Reference Map Theory

The RMT is a continuum mechanics method which is framed in an Eulerian reference frame. The sea ice dynamics model developed in this thesis is based on the RMT, as presented by Rycroft et al. [37]. The RMT is based on mapping the deformed configuration $\mathcal{B}_t$ from the initial (undeformed) configuration $\mathcal{B}$ of the solid as $\boldsymbol{\chi} : \mathcal{B} \times \mathbb{R} \to \Omega$ where $t \in \mathbb{R}$ is the time and Ω is the physical domain. Accordingly, each material point $\mathbf{X} \in \mathcal{B}$ is related to its placement $\mathbf{x}$ in the deformed configuration $\mathcal{B}_t$ by the following equation of motion

$$\mathbf{x} = \boldsymbol{\chi}(\mathbf{X}, t) \tag{3.1}$$

which is illustrated in Fig. 3.1.

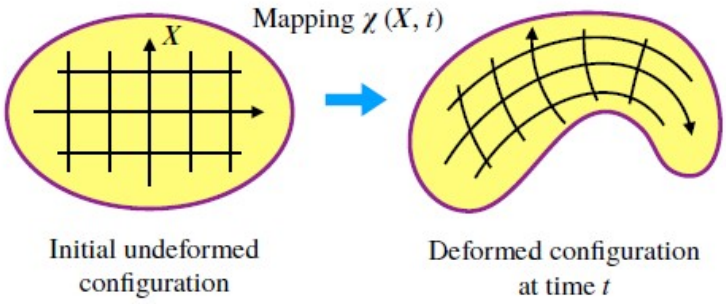

Figure 3.1: An overview of the reference map applied to a hyperelastic framework, reproduced from Rycroft et al. [37].

In what follows, without loss of generality, we identify the body $\mathcal{B}$ with its undeformed reference configuration at fixed time t_0. The reference map, $\boldsymbol{\xi}(\boldsymbol{x}, t)$, is defined as the inverse of the motion function $\boldsymbol{\chi}_t$ [15],

$$\boldsymbol{X} = \boldsymbol{\xi}(\boldsymbol{x}, t). \tag{3.2}$$

The deformation map possesses an invertible linear tangent map, the so-called deformation gradient tensor, defined as

$$\boldsymbol{F} = \frac{\partial \boldsymbol{\chi}}{\partial \boldsymbol{X}}, \tag{3.3}$$

where the Jacobian $J = \det \mathbf{F} > 0$. With Eq. (3.2) the inverse of the deformation gradient can be expressed as

$$\mathbf{F}^{-1} = \frac{\partial \boldsymbol{\xi}}{\partial \mathbf{x}}. \tag{3.4}$$

The reference map $\boldsymbol{\xi}$ is a primary variable which is solved in the deformed configuration and the deformation gradient $\mathbf{F}$ is subsequently obtained by inverting the spatial gradient of the reference map (Eq. (3.4)).

With deformation gradient determined, any classical constitutive laws used in solid mechanics can be utilized. For later use, we introduce here the Neo-Hookean hyperelastic constitutive law with the Cauchy stress tensor given by

$$\boldsymbol{\sigma}_s = f(\mathbf{F}) = G\left(J^{-1}\right)^{\frac{5}{3}}\mathbf{b} + \left(K(J-1) - \frac{1}{3}G(J^{-1})^{\frac{5}{3}}(1 - tr(\mathbf{b}))\right)\boldsymbol{I}, \tag{3.5}$$

where $\mathbf{b} = \mathbf{F}\mathbf{F}^T$ denotes the left Cauchy-Green deformation tensor, G is the shear modulus and K is the bulk modulus. The Cauchy stress in the fluid is computed by

$$\boldsymbol{\sigma}_f = g(\mathbf{u}, p) = 2\mu\epsilon(\mathbf{u}) - pI, \tag{3.6}$$

where $\mathbf{u}(\mathbf{x}, t)$ denotes the velocity field which is second primary variable besides the reference map, p is the pressure field in the fluid, and the strain rate tensor, $\epsilon(\mathbf{u})$, is defined as

$$\epsilon(\mathbf{u}) = \frac{1}{2}\left(\nabla\mathbf{u} + (\nabla\mathbf{u})^T\right). \tag{3.7}$$

The reference map is updated in the Eulerian frame using advection equation,

$$\frac{\partial\boldsymbol{\xi}}{\partial t} + (\boldsymbol{u}\cdot\nabla)\,\boldsymbol{\xi} = \mathbf{0}. \tag{3.8}$$

The velocity field is governed by the conservation of linear momentum,

$$\rho\left(\frac{\partial\boldsymbol{u}}{\partial t} + (\boldsymbol{u}\cdot\nabla)\,\boldsymbol{u}\right) = \nabla\cdot\boldsymbol{\sigma}, \tag{3.9}$$

where, in this case, $\rho(\mathbf{x}, t)$ is the density in the deformed configuration which is conserved in time[37]. The equations (3.3) - (3.9) form the basic system of equations for a finite-strain hyperelastic framework based purely in an Eulerian frame [37]. This is a general method to solving the FSI problem with the RMT, which is schematically illustrated in Fig. 3.2. The corresponding numerical schemes are described in the following section [37].

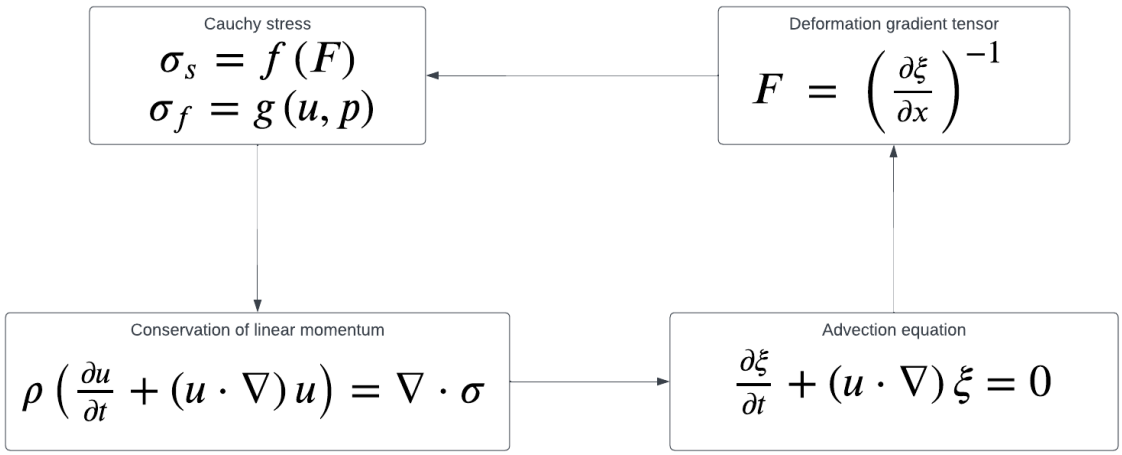

Figure 3.2: General process used to solve hyperelastic FSI problems with the reference map technique [37].

Chapter 4

Implementation of the Reference Map Technique

This chapter describes the approach used to develop an FSI model in FEniCS and separate complementary C++ code to simulate sea ice dynamics problems. FEniCS is an open-source finite element library which allows for automated solving of differential equations [18]. A unique modelling technique is explained that builds on previous work [37] and is applied to sea ice behaviour found in Antarctica which, at the time of this research and to the knowledge of the researchers involved, has not yet been performed in this manner. This model is easily adaptable and is not limited to applications in Antarctic sea ice dynamics, but rather it can accommodate a range FSI applications in two-dimensions.

The model is sorted into three groups: the fluid model, the solid model and the interface model. The fluid model is solved over the entire domain using finite elements, coupled to the solid model via the drag forcing. The solid model is only solved on a specific patches of the domain as defined by a level-set function using a finite difference scheme. The interface model couples the two systems and handles the transfer of velocity/forces between the two. The level-set function is described from the update of the reference map and is an implicit method for describing moving interfaces.

4.1 Research Assumptions and Available Software

The study assumed that thermodynamic effects on the sea ice, regarding ice thickness and concentration, are negligible in comparison to dynamic effects on a short time scale [22]. Ice floe ridging was disregarded and assumed to be negligible [22]. Therefore, the model was simplified to a two-dimensional case in which a 'bird's-eye-view' perspective was modelled.

The open-source finite element modelling (FEM) computational platform which is used for solving differential equations, the FEniCS Project, was used to design the fluid model [17]. FEniCS is primarily written in Python thus the fluid code is written in Python. A C++ code was written from scratch to account for the solid computation and extrapolation. The two models are coupled using a Ctypes library [9] which accommodates the interface between the two coding languages, Python and C++.

4.2 Momentum Balance and Reference Map Update

The solid and fluid velocity satisfies the conservation of linear momentum. The solid momentum equation is defined as follows, with a positive contribution of drag:

$$\rho_s \left(\frac{\partial \boldsymbol{u}_s}{\partial t} + (\boldsymbol{u}_s \cdot \nabla)\, \boldsymbol{u}_s \right) = \nabla \cdot \boldsymbol{\sigma}_s + \psi(\boldsymbol{u}_s - \boldsymbol{u}), \tag{4.1}$$

where $\boldsymbol{\sigma}_s$ is the solid stress, ψ is some drag coefficient between solid and fluid, $\boldsymbol{u}_s$ is the solid velocity, $\boldsymbol{u}$ is the fluid velocity and ρ_s is the undeformed solid density [37]. The fluid momentum equation subsequently has a negative drag contribution in order to remain conservative:

$$\rho_f \left(\frac{\partial \boldsymbol{u}}{\partial t} + (\boldsymbol{u} \cdot \nabla)\, \boldsymbol{u} \right) = \nabla \cdot \boldsymbol{\sigma}_f - \psi(\boldsymbol{u}_s - \boldsymbol{u}), \tag{4.2}$$

where ρ_f is the fluid density and $\boldsymbol{\sigma}_f$ is the fluid stress. The drag is assumed to be linear due to the relatively low velocities expected in the model. The incompressibility constraint is applied to the fluid to adhere to the Navier-Stokes system of equations. For an incompressible fluid model on the ocean surface, the incompressibility constraint is modified to:

$$\nabla \cdot \boldsymbol{u} = s \tag{4.3}$$

in order to account for the effect of this small-amplitude plane wave, where s is the wave forcing term that captures the upwelling and downwelling of the the ocean surface for small amplitude gravity waves. The background for the wave source term is shown in the following section.

A reference map is introduced in the physical frame, $\boldsymbol{\xi}(\boldsymbol{x}, t)$ which represents the inverse mapping of $\boldsymbol{\chi}$. The field is initialised at $\boldsymbol{\xi}(\boldsymbol{x}, 0) = \boldsymbol{x}$, the spatial coordinates, and satisfies the advection equation (4.4):

$$\frac{\partial \boldsymbol{\xi}}{\partial t} + (\boldsymbol{u} \cdot \nabla)\, \boldsymbol{\xi} = \boldsymbol{0}. \tag{4.4}$$

The updated reference map is evaluated and inputted into (4.5) in order to find the new deformation gradient tensor,

$$\boldsymbol{F} = \left(\frac{\partial \boldsymbol{\xi}}{\partial \boldsymbol{x}} \right)^{-1}. \tag{4.5}$$

4.3 Wave Forcing

Consider a periodic square domain of length L representing a patch of the ocean surface [36]. Let $\eta(x, y, t)$ be the height of the ocean surface over time. The bulk velocity is given as $\boldsymbol{u} = \nabla \boldsymbol{\phi}$, using a bulk potential function, $\boldsymbol{\phi}(x, y, z, t)$. The free surface height satisfies the

partial differential equation,

$$\eta_t = \phi_z - \eta_x \phi_x - \eta_y \phi_y. \tag{4.6}$$

Let $\boldsymbol{\varphi}(x, y, t) = \boldsymbol{\phi}(x, y, \eta(x, y, t), t)$ be the restriction of the velocity potential to the free surface, thus, from the Bernoulli equation, the surface velocity potential satisfies:

$$\boldsymbol{\varphi}_t = P\left[\phi_z \eta_t - \frac{|\nabla \boldsymbol{\phi}|^2}{2} - \eta \boldsymbol{g}\right], \tag{4.7}$$

where $\mathbf{g}$ is gravitational acceleration and P is the projection operator, ensuring that the right hand side has zero mean. In order to evaluate the Eqs. (4.6) and (4.7) at each time step, ϕ_z needs to be found which requires solving the Laplace equation,

$$\nabla \cdot \boldsymbol{u} = \nabla^2 \boldsymbol{\phi} = 0, \tag{4.8}$$

in the bulk of the fluid where $z < \eta$ and subject to the boundary condition that $\boldsymbol{\phi} = \boldsymbol{\varphi}$ when $z = \eta$.

To find small amplitude solutions, define the surface height as

$$\eta = \epsilon \exp\left(i\left(\frac{jx + ky}{L} - \omega t\right)\right), \tag{4.9}$$

for wave modes $j, k \in Z$, where the real part corresponds to the physical solution. In Eq. (4.9), ϵ is a small parameter with dimension of length, and ω is frequency.

Assume that $\boldsymbol{\phi}$ is $O(\epsilon)$ and solutions to Eqs. 4.6 and 4.7 neglect all $O(\epsilon^2)$ terms, the equations then simplify to

$$\eta_t = \phi_z, \tag{4.10}$$

$$\boldsymbol{\varphi}_t = -\eta g. \tag{4.11}$$

Since $\boldsymbol{\varphi}(x, y, t) = \boldsymbol{\phi}(x, y, 0, t) + O(\epsilon^2)$, a solution to Eq. 4.8 in the semi-infinite domain $z < 0$ can be considered. We search for a separable solution,

$$\boldsymbol{\phi}(x, y, z, t) = -i\epsilon F(z) \exp\left(i\left(\frac{jx + ky}{L} - \omega t\right)\right), \tag{4.12}$$

where $F(z)$ is an arbitrary function of z, and the additional $-i$ factor has been incorporated for convenience. Let $\mu_{jk}^2 = (j^2 + k^2)/L^2$, then the Laplace equation becomes

$$0 = \nabla^2 \boldsymbol{\phi} = \phi_{xx} + \phi_{yy} + \phi_{zz} = \frac{-F(z)\mu_{jk}^2 + F''(z)}{F(z)} \boldsymbol{\phi} \tag{4.13}$$

and thus

$$F(z)\mu_{jk}^2 = F''(z). \tag{4.14}$$

The general solution for this is

$$F(z) = Ae^{-\mu_{jk}z} + Be^{\mu_{jk}z} \tag{4.15}$$

and in order for $F(z)$ to be bounded as $z \to -\infty$, it must be that $A = 0$. Therefore

$$\boldsymbol{\phi}(x, y, z, t) = -Bi\epsilon \exp\left(i\left(\frac{jx + ky}{L} - \omega t\right) + \mu_{jk}z\right) \tag{4.16}$$

and

$$\phi_z = -Bi\mu_{jk}\epsilon \exp\left(i\left(\frac{jx + ky}{L} - \omega t\right) + \mu_{jk}z\right). \tag{4.17}$$

Following on from Eq. 4.10,

$$i\omega = Bi\mu_{jk}, \tag{4.18}$$

and from Eq. 4.11

$$B\omega = g. \tag{4.19}$$

Substituting μ_{jk}, it is found that

$$B = \frac{\omega L}{j^2 + k^2} \tag{4.20}$$

and

$$\omega = \sqrt{\frac{g(j^2 + k^2)}{L}}. \tag{4.21}$$

The in-plane surface velocity takes the form

$$\boldsymbol{u}_{surf} = (\phi_x, \phi_y) = \left(\frac{j}{L}, \frac{k}{L}\right) \times B\epsilon \exp\left(i\left(\frac{jx + ky}{L} - \omega t\right)\right). \tag{4.22}$$

The divergence of the velocity can be calculated as follows:

$$\begin{aligned} s(x, y, t) = \nabla \cdot \boldsymbol{u}_{surf} &= \phi_{xx} + \phi_{yy} \\ &= -\phi_{zz} \\ &= -Bi\mu_{jk}^2\epsilon \exp\left(i\left(\frac{jx + ky}{L} - \omega t\right) + \mu_{jk}z\right) \\ &= -\frac{\omega\epsilon i}{L} \exp\left(i\left(\frac{jx + ky}{L} - \omega t\right) + \mu_{jk}z\right) \\ &= -\frac{\omega\epsilon i}{L} \exp\left(\mu_{jk}z\right)\left(\cos\left(\frac{jx + ky}{L} - \omega t\right) + i\sin\left(\frac{jx + ky}{L} - \omega t\right)\right), \end{aligned} \tag{4.23}$$

of which the real part is taken to be the physical representation of gravity waves.

4.4 Numerical Method

The numerical method is broken up into solid and fluid constituents, with a coupling between them. Figure 4.1 shows the code structure used for the simulation and Figure 4.2 shows the solid domain set up.

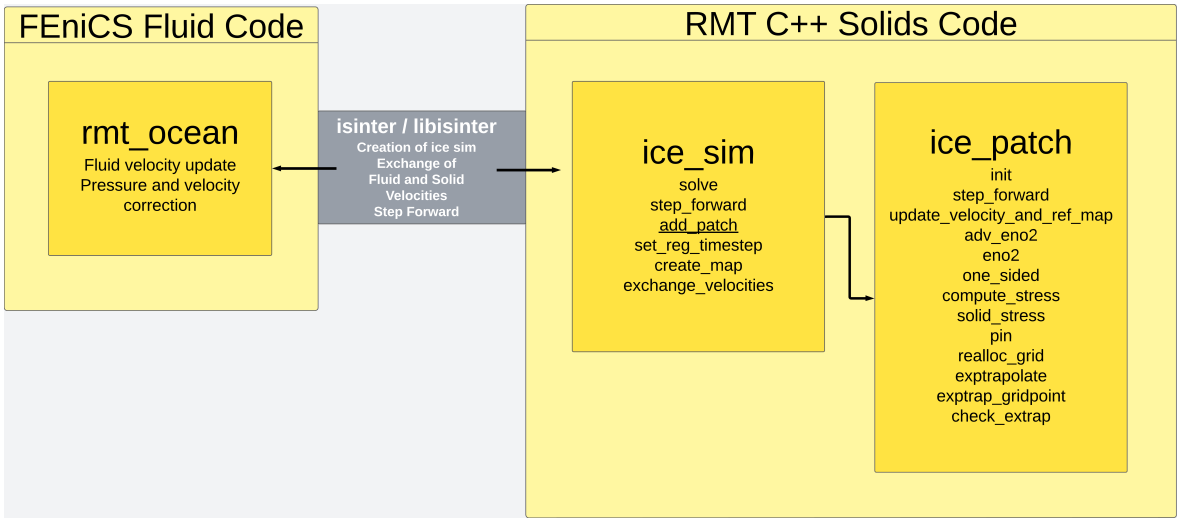

Figure 4.1: Flow chart showing the main code used in the FSI model.

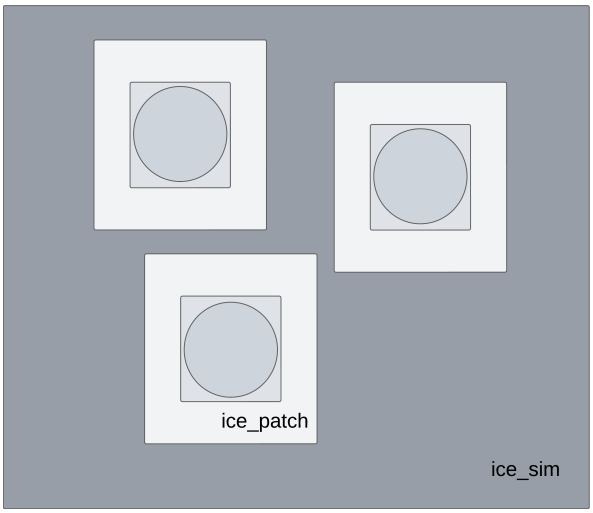

Figure 4.2: Diagram showing the set up of the solid domains.

4.4.1 Mesh Generation, Function Spaces and Boundaries

The model domain is constructed on a 60 m by 60 m grid, with 0.5 m by 0.5 m quadrilateral elements. The domain boundaries are divided into top, bottom, inlet (left) and outlet (right) and are set to be periodic in both the lateral and transverse directions.

The simulation domain can be made rectangular, with width W and height H, divided into a general fixed grid of $M \times N$ cells. The cells are indexed according to standard matrix indexing with $i = 0, \ldots, M-1$ and $j = 0, \ldots, N-1$. The reference map, velocity and level set values in the solid model are computed at the cell centres, and the stress and pressure in the fluid model are computed at cell corners [37]. Subscripts denote the position on the grid where as superscripts represent the time steps.

There are four function spaces created for the primary and secondary variables in the fluid model. The first primary variable, velocity, has a vector function space with Lagrange elements of degree two assigned to it. The second primary variable, the coordinate map field, also has a vector function space with Lagrange elements of degree two. The secondary variables, stress and pressure, have Langrange elements of degree one for the tensor function space and scalar function space, respectively. Each of these variables are assigned test and trial functions.

4.4.2 Modelling Grease Ice as Fluid Flow - The Projection Method

The fluid model uses an example from the FEniCS Tutorial Volume I [18], which used the incompressible Navier-Stokes equations to simulate fluid flow. The approach uses the splitting method by Chorin [4, 5] with certain modifications. For improved accuracy we make use of the incremental pressure correction scheme. The Navier-Stokes equations are solved using three linear variation problems every time step.

Firstly, a tentative velocity, $\boldsymbol{u}^\star$, is found from advancing the fluid momentum equation 4.2 in time, using a midpoint finite difference scheme and the pressure from the previous time step. The non-linear convective term of 4.2, $\boldsymbol{u}^n \cdot \nabla \boldsymbol{u}^n$, is linearized using the known velocity of the previous time interval. The first variational problem is

$$\begin{aligned} \langle \frac{\rho_f(\boldsymbol{u}^\star - \boldsymbol{u}^n)}{\Delta t}, \boldsymbol{v} \rangle + \langle \rho_f \boldsymbol{u}^n \cdot \nabla \boldsymbol{u}^n, v \rangle + \langle \boldsymbol{\sigma}_f(\boldsymbol{u}^{n+\frac{1}{2}}, p^n), \epsilon(\boldsymbol{v}) \rangle \\ + \langle p^n n, \boldsymbol{v} \rangle_{\partial\Omega} - \langle \mu \nabla \boldsymbol{u}^{n+\frac{1}{2}} \cdot n, \boldsymbol{v} \rangle_{\partial\Omega} = \langle f^{n+1}, \boldsymbol{v} \rangle + \langle \psi(\boldsymbol{u}_s^n - \boldsymbol{u}^n), \boldsymbol{v} \rangle, \end{aligned} \tag{4.24}$$

where $\boldsymbol{v}$ is the vector test function and $\boldsymbol{u}^{n+\frac{1}{2}} \approx (\boldsymbol{u}^n + \boldsymbol{u}^{n+1})/2$. The short-hand notation corresponds to

$$\langle \boldsymbol{v}, \boldsymbol{w} \rangle = \int_\Omega \boldsymbol{v}\boldsymbol{w} d\boldsymbol{x}, \quad \langle \boldsymbol{v}, \boldsymbol{w} \rangle_{\partial\Omega} = \int_{\partial\Omega} \boldsymbol{v}\boldsymbol{w} ds. \tag{4.25}$$

Side note: The integration by parts of the divergence of stress term, $\langle -\nabla \cdot \boldsymbol{\sigma}, \boldsymbol{v} \rangle$, is made up of both surface traction and boundary traction:

$$\langle -\nabla \cdot \boldsymbol{\sigma}, \boldsymbol{v} \rangle = \langle \boldsymbol{\sigma}, \epsilon(\boldsymbol{v}) \rangle - \langle T, \boldsymbol{v} \rangle_{\partial\Omega}. \tag{4.26}$$

But in this method, we use a free boundary thus $T = 0$ on the boundary. However, to ensure we are modelling a situation where the outflow corresponds to a fully developed flow that does not significantly change outside of the domain, the resulting boundary term is $pn - \mu \nabla \boldsymbol{u} \cdot n$.

Using the tentative velocity, $\boldsymbol{u}^\star$, the current pressure is computed by taking the difference in the previous time step momentum equation and the current time step equation,

$$\frac{(\boldsymbol{u}^{n+1} - \boldsymbol{u}^\star)}{\Delta t} + \nabla p^{n+1} - \nabla p^n = 0. \tag{4.27}$$

Applying the modified incompressibility constraint ($\nabla \cdot \boldsymbol{u}^{n+1} = s$) results in the Poisson problem for pressure

$$\frac{s}{\Delta t} - \frac{\nabla \cdot \boldsymbol{u}^\star}{\Delta t} + \nabla^2 p^{n+1} - \nabla^2 p^n = 0 \tag{4.28}$$

from which we can solve for the updated pressure. The pressure is solved in variational form with

$$\langle \nabla p^{n+1}, \nabla q \rangle = \langle \nabla p^n, \nabla q \rangle - \frac{1}{\Delta t} \langle \nabla \cdot \boldsymbol{u}^\star, q \rangle - \frac{1}{\Delta t} \langle s, q \rangle, \tag{4.29}$$

where q is the scalar test function. The corrected velocity for the current time step is then updated using

$$\langle \boldsymbol{u}^{n+1}, \boldsymbol{v} \rangle = \langle \boldsymbol{u}^\star, \boldsymbol{v} \rangle - \Delta t \langle \nabla (p^{n+1} - p^n), \boldsymbol{v} \rangle. \tag{4.30}$$

The incompressibility constraint looks slightly different as it has a wave source term, although it does not change the way the fluid flow problem is solved. Table 4.1 summarises the preconditioners and solvers used for solving the linearized set of equations for incompressible Navier-Stokes fluid flow.

Table 4.1: Showing the solvers and preconditioners used for the three linear variational problems for each time step.

Equation	Solver	Preconditioner
4.24	Biconjugate gradient stabilized method	High performance algebraic multi-grid method
4.29	Biconjugate gradient stabilized method	High performance algebraic multi-grid method
4.30	Conjugate gradient method	Successive over-relaxation method

4.4.3 Reference Map Initialisation and Level Set Method

The initial coordinates of the reference map field mask the initial cartesian coordinates of the simulation domain. The reference map needs to be initialised before the level set method is implemented in order for the signed distance function to track the movement of the solid boundaries over time.

The first step of the level set method is to construct a signed distance function. The signed distance function outputs a field of points for the entire domain that correspond to the shortest distance to the outer edge of the solid objects, with points on the edge evaluating to zero,

points inside the object evaluating to positive numbers and points outside evaluating to negative numbers. From the signed distance function, a Heaviside function can be constructed.

A level set function, $\phi(\boldsymbol{x}, t)$, is used at the fluid-solid interface to indicate the boundary separating the fluid and solid components. The level set function computes a sign-sensitive distance from the fluid-solid interface at each point within a band called the blur zone. The convention will be that the level set value is greater than zero in the solid and less than zero in the fluid. The level set field will not be explicitly updated, rather it will be tied to the reference map update [37].

4.4.4 Solid Stress

In the solid model, a staggered grid approach is used, where the variables are stored at different grid locations. The velocity, level set and reference map values are stored at cell centres where as the pressure and stress is stored at cell corners [37]. To evaluate advective terms at half-time steps, the half indexed velocities and reference map values are stored on the cell edges as shown in Fig. 4.3.

The Jacobian components are calculated using the second-order finite-difference formulae:

$$\left(\frac{\partial \boldsymbol{\xi}}{\partial x}\right)_{i-\frac{1}{2},j} = \frac{\boldsymbol{\xi}_{i,j} - \boldsymbol{\xi}_{i-1,j}}{h_x} \tag{4.31}$$

and

$$\left(\frac{\partial \boldsymbol{\xi}}{\partial y}\right)_{i-\frac{1}{2},j} = \frac{\boldsymbol{\xi}_{i,j+1} + \boldsymbol{\xi}_{i-1,j+1} - \boldsymbol{\xi}_{i,j-1} - \boldsymbol{\xi}_{i-1,j-1}}{4h_y} \tag{4.32}$$

The deformation gradient is then evaluated using the following:

$$\boldsymbol{F}_{i-\frac{1}{2},j} = \left(\left(\frac{\partial \boldsymbol{\xi}}{\partial \boldsymbol{x}}\right)_{i-\frac{1}{2},j}\right)^{-1} \tag{4.33}$$

The compressible neo-Hookean material law (Eq. (3.5)) is then used to calculate the solid stresses with the Jacobian, $J = \det(F)$.

4.4.5 Extrapolation

The reference map and solid velocity values need to be extended out of each solid in order to perform the stress calculations at the edges of the solid. More generally, extrapolation of the fields is necessary in order to have enough points available to perform the finite-difference updates. This is done using a unique extrapolation technique.

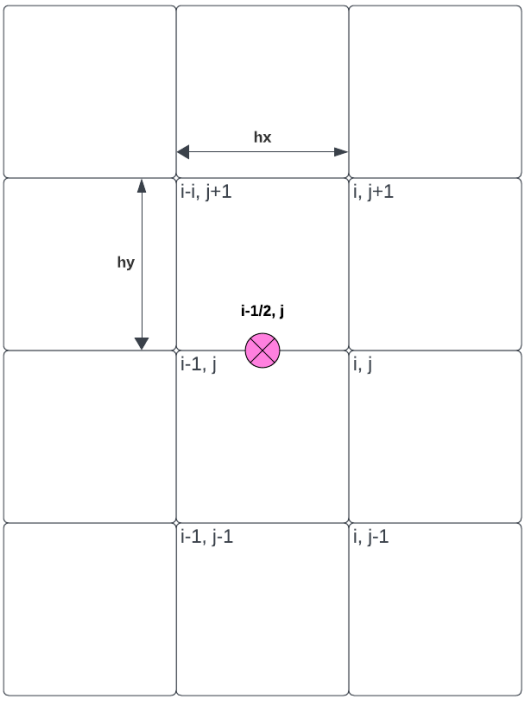

Figure 4.3: Diagram showing the stencil of the finite difference method used to get the edge values of the reference map[37].

During the level set construction, a list of grid points that lie near the solid edge region is constructed.

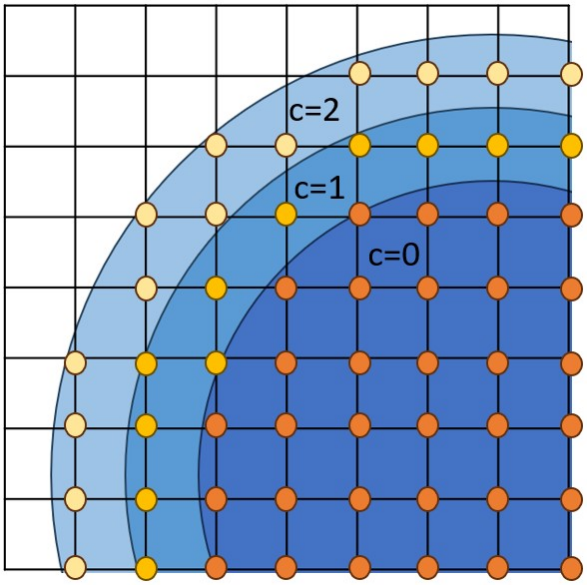

Figure 4.4: Diagram showing a solid with two extrapolated layers, where c is an indicator function showing layers of extrapolation.

An indicator function, c, shows which grid points are inside the ice patch/solid at the current time step and updates the velocity and reference map values inside the patch only. If the grid point lies in the interior solid region, the neighbouring points are checked to see if there are any points lying outside the solid. If there is an exterior point, the point is marked and extrapolated, and a layer around the solid is created. The routine is repeated until the desired number of extrapolation layers is created. Figure 4.4 shows an example of how the extrapolation layers are created. All the points in $c = 1$ are set based on extrapolating from $c = 0$. Then all the points in $c = 2$ are set based on extrapolating from $c \in \{0, 1\}$. The extrapolation routine fills in the values of the reference map and velocity of the neighbouring cells after the update step. The 'pin' routine (refer to Fig 4.1) recomputes the level set to reassign which values lie within the solid regions.

Since the method uses all the neighbouring values and averaging, it results in significant blurring when the extrapolation occurs far from the interface. Although, in this case, only values near the interface are used and the averaging serves as a dampener for instabilities. This approach makes it possible to implement solid objects with sharp corners such as squares and rectangles.

4.4.6 Parameters and Stability

The model has four main material parameters: fluid viscosity μ_f, fluid density ρ_f, solid shear modulus G (derived from the solid bulk modulus, K, and Poisson's ratio, ν), and solid density ρ_s. There are two time step conditions that need to be considered. Firstly, in the solid structures, the compressive wave speed will be $c_c = \sqrt{K/\rho_s}$. The Courant-Friedrichs-Lewy (CFL) condition requires a simulation time step that is less than or equal to

$$\Delta t_I \leq \frac{1}{c_c} \min\{h_x, h_y\} = \sqrt{\frac{\rho_s}{K}} \min\{h_x, h_y\}. \tag{4.34}$$

Secondly, using the von Neumann stability analysis in order to resolve the viscous fluid stress [37], the time step must be less than or equal to

$$\Delta t_{II} = \frac{\rho_f}{2\mu_f \left(h_x^{-2} + h_y^{-2}\right)} \tag{4.35}$$

Therefore, the maximum time step is based on the CFL condition and von Neumann stability analysis. The smallest of these time-steps is used as the maximum time step for the simulation with a safety factor applied to it. The solid may encounter instabilities, especially if it has a relatively high elastic modulus. Thus, a small artificial viscous stress is added inside the solid which should satisfy

$$\mu_e = \kappa_e \rho_s c_s \max\{h_x, h_y\} \tag{4.36}$$

where κ_e is a dimensionless constant. It was found that the artificial viscous stress also aids in dampening the fluid-solid interface region [37].

Furthermore, for more realistic sea ice dynamics applications, where the solids have a significantly higher stiffness, the solid model would require much smaller time steps than the fluid simulation. A sub-stepping regime was implemented which allows the solid model to have multiple time steps for every one fluid model time step.

Chapter 5

Case Studies and Discussion

The parameters used in this model have been chosen to suit the application to sea ice at a small scale but it is not limited to this application. This model primarily serves as an initial proof of concept showing the potential for the use of the RMT in a FSI sea ice dynamics model.

This chapter presents and discusses various case studies including the verification of the various components of the model. The simulations were run on a Dell XPS 13 9320/Core i7-1260P/16GB/512GB SSD/13.4" laptop with Ubuntu 23.04 Linux operating system.

5.1 Verification of Model

The model was tested for convergence to study the accuracy of the numerical method. Three cases were assessed in the mesh independence study, Fluid Only, Solid Only, and Coupled Fluid-Solid Interaction on a periodic domain of $60\,\mathrm{m} \times 60\,\mathrm{m}$. Dimensionless parameters were used similar to Rycroft et al. [37]. An initial velocity field was applied to the models, Fluid Only and Coupled Fluid-Solid Interaction, which follows:

$$\boldsymbol{u}_{twist}(\boldsymbol{x}) = \left(-y \exp\left(-\frac{(x-40\,\mathrm{m})^2 + (y-20\,\mathrm{m})^2}{50\,\mathrm{m}^2}\right), x \exp\left(-\frac{(x-40\,\mathrm{m})^2 + (y-20\,\mathrm{m})^2}{50\,\mathrm{m}^2}\right)\right). \tag{5.1}$$

The tests were carried out over a simulation time up to $t = 0.5s$. The time step selection adheres to the CFL condition described in section 4.4 with a safety factor of 0.25, which reduces the time step well below the limit. Six different grid resolutions were chosen ranging from 30×30 to 300×300 quadrilateral elements. All simulations had periodic boundary conditions (BCs).

5.1.1 Fluid Only Convergence Study

The L^2 error norm of the fluid velocity was used to compare the accuracy of grid resolution. The parameters used in the Fluid Only case are summarised in Table 5.1 and chosen to follow the parameters used for the convergence test in [37]. The table contains the bulk and shear moduli to inform the CFL condition restriction for the time step.

Table 5.1: Parameters used for Fluid Only convergence test.

Final time, T	0.5 s
Time step, dt	0.05 s
Fluid density, ρ_f	1 kg/m^3
Dynamic viscosity, μ	50 Pa s
Bulk modulus, K	2 N/m^2
Shear modulus, G	1 N/m^2
Domain length, L	60 m
Domain width, W	60 m
Element sizes, h	[0.2, 0.25, 0.4, 0.5, 1.0, 2.0] m

Fig. 5.1 shows the error norms for each of the six grid resolutions over the time period. It was required to compare the error between the element sizes for the fixed domain size. For this, the maximum resolution grid is used as the reference and the difference between all the other resolutions are compared against it,

$$\text{Error} = \|\boldsymbol{u} - \boldsymbol{u}_{\text{ref}}\|_2. \tag{5.2}$$

where $\boldsymbol{u}$ is the fluid velocity and $\boldsymbol{u}_{ref}$ is the reference fluid velocity from the most refined mesh. Therefore, Fig. 5.1 shows the fluid velocity error with respect to the reference fluid velocity of the 300×300 element grid. As expected, the error norm is zero at $t = 0$ s as the applied velocity profile has rotational symmetry. The error then spikes and settles by $t = 0.5$ s. As shown, the error norm significantly decreases as the resolution of the grid increases.

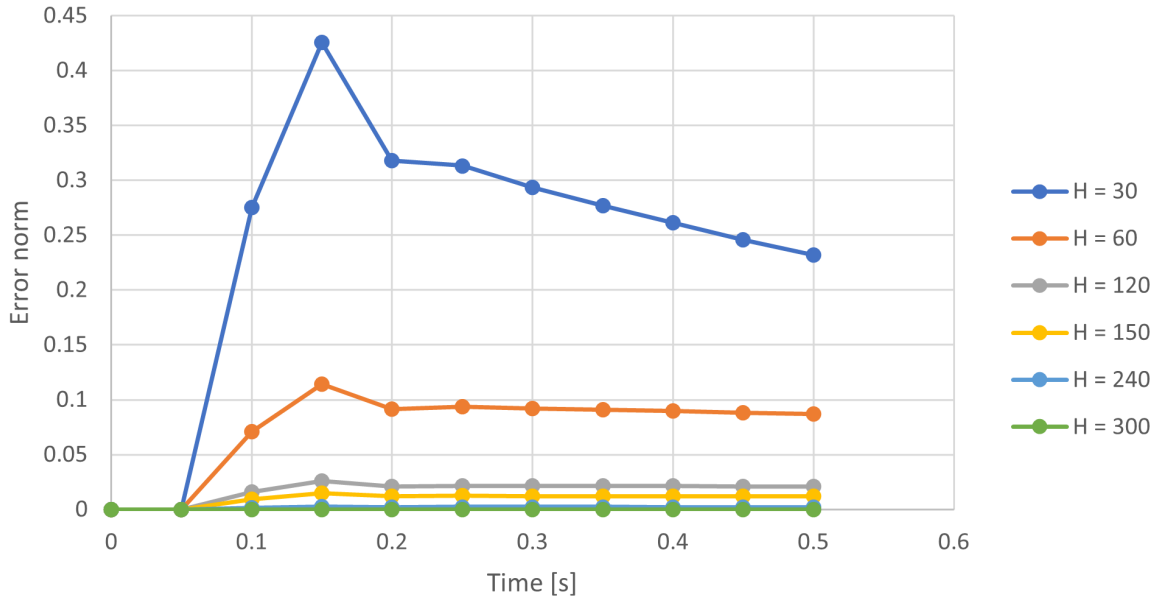

Figure 5.1: Fluid Only convergence test showing the L2 velocity error norms of various grid refinements, H, over the period of 0.5 seconds.

5.1.2 Solid Only Convergence Study

The L^2 norm of the solid velocity was used to compare the accuracy of grid resolution. The parameters used in the Solid Only case are summarised in Tab. 5.2. The solid was given an initial velocity of 1 m/s to the right.

Table 5.2: Parameters used for Solid Only convergence test.

Final time, T	0.5 s
Time step, dt	0.05 s
Solid density, ρ_s	$1\,\mathrm{kg/m^3}$
Dynamic viscosity, μ	50 Pa s
Bulk modulus, K	$2\,\mathrm{N/m^2}$
Shear modulus, G	$1\,\mathrm{N/m^2}$
Domain length, L	60 m
Domain width, W	60 m
Element sizes, h	[0.2, 0.25, 0.4, 0.5, 1.0, 2.0] m

Fig. 5.2 shows the error norms for each of the six grid resolutions over the time period. It shows the error norm with respect to the reference norm of the 300×300 element grid. As expected, the error significantly decreases as the resolution of the grid increases.

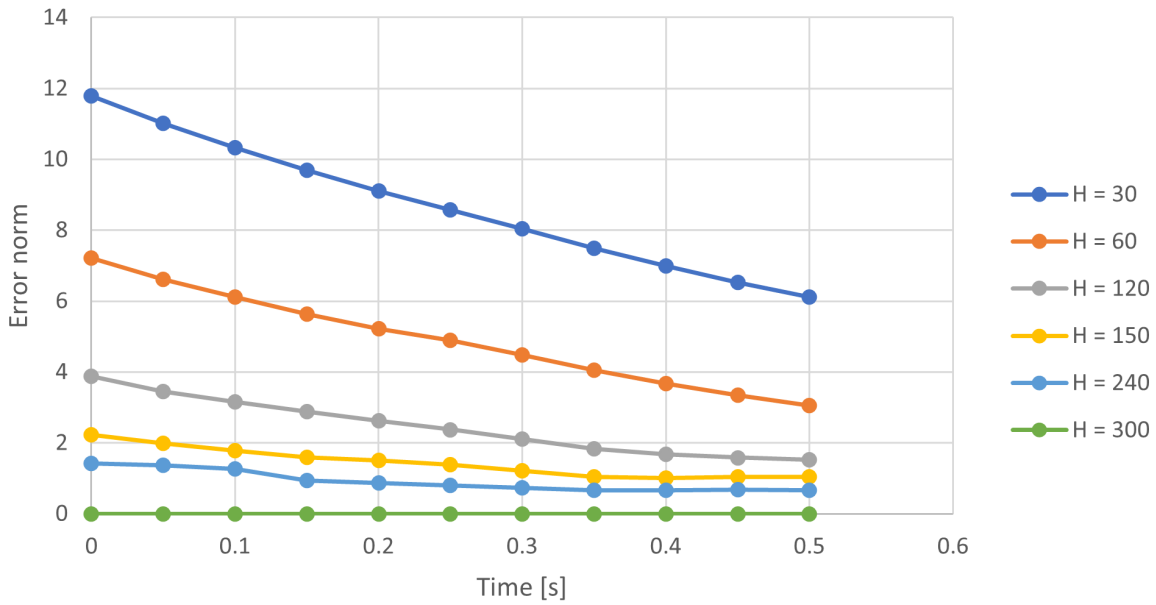

Figure 5.2: Solid Only convergence test showing the L^2 solid velocity error norms of various grid refinements, H, over the period of 0.5 seconds.

5.1.3 Coupled Fluid-Solid Interaction Convergence Study

For this case, the solid and fluid models were coupled by adding a single circular solid object of diameter $30m$ into the centre of the fluid domain and applying the same $\boldsymbol{u}_{twist}$ velocity as the Fluid Only case. The L^2 error norms of the fluid velocity and the solid velocity was used to compare the accuracy of grid resolution in this case study. The parameters used in the case are summarised in Tab. 5.3 below.

Table 5.3: Parameters used for FSI convergence test.

Final time, T	$0.5\,\mathrm{s}$
Time step, dt	$0.05\,\mathrm{s}$
Fluid density, ρ_f	$1\,\mathrm{kg/m^3}$
Solid density, ρ_s	$1\,\mathrm{kg/m^3}$
Dynamic viscosity, μ	$50\,\mathrm{Pa\,s}$
Bulk modulus, K	$2\,\mathrm{N/m^2}$
Shear modulus, G	$1\,\mathrm{N/m^2}$
Skin drag coefficient, ψ_{skin}	1
Form drag coefficient, ψ_{form}	1
Domain length, L	$60\,\mathrm{m}$
Domain width, W	$60\,\mathrm{m}$
Element sizes, h	[0.2, 0.25, 0.4, 0.5, 1.0, 2.0] m

As seen for the Fluid Only convergence case, similar values and orders of magnitude for the error norms were found. Fig. 5.3 shows the fluid error norms for each of the six grid resolutions over the time period. A decrease in fluid velocity error as the grid is refined is seen.

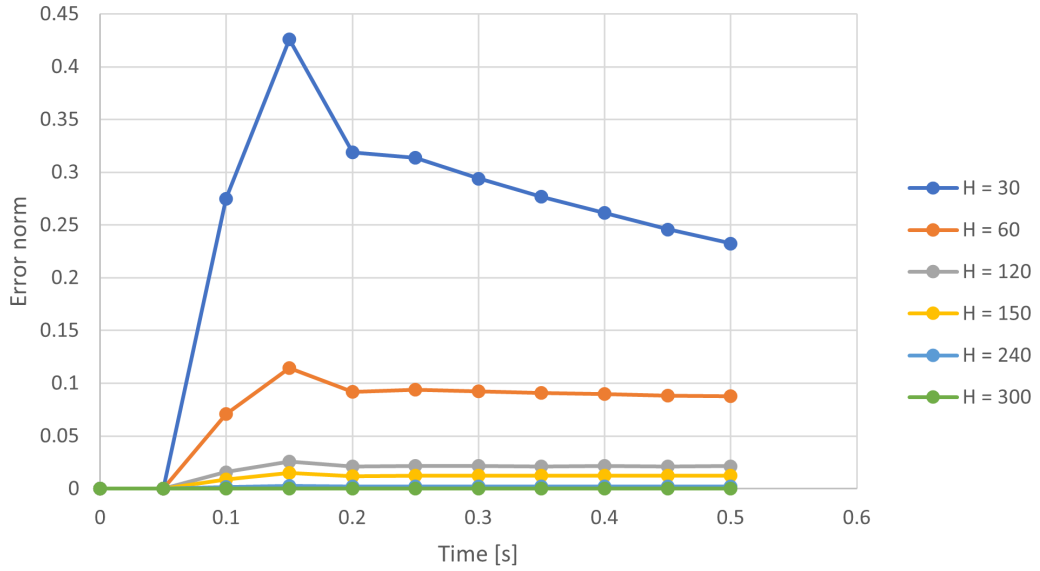

Figure 5.3: Fluid convergence test for the Coupled FSI case showing the L2 velocity error norms of various grid refinements, H, over the period of 0.5 seconds.

Fig. 5.4 shows the error norms of the solid velocity for each of the six grid resolutions over the time period. A decrease in the solid velocity error as the grid is refined is seen.

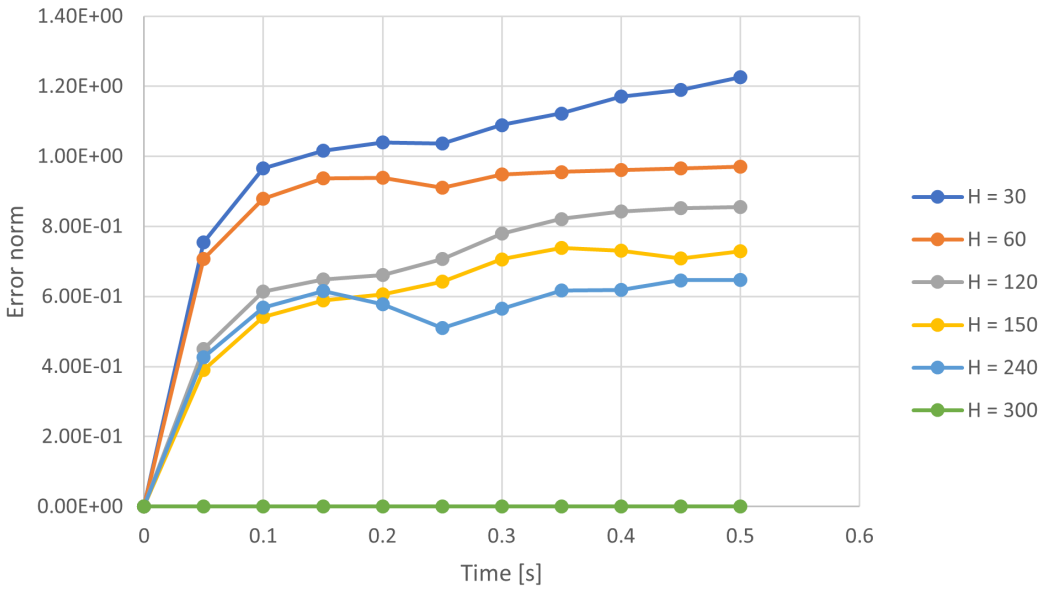

Figure 5.4: Solid convergence test for the Coupled FSI case showing the L2 velocity error norms of various grid refinements, H, over the period of 0.5 seconds.

In summary, Fig. 5.5 shows the relationship between the error norm and grid size for all test cases at $t = 0.5\,\mathrm{s}$. This shows that the model converges at a rate of h^2 and that the convergence results are in accordance with the convergence results of [37] (shown in Appendix

B of [37]).

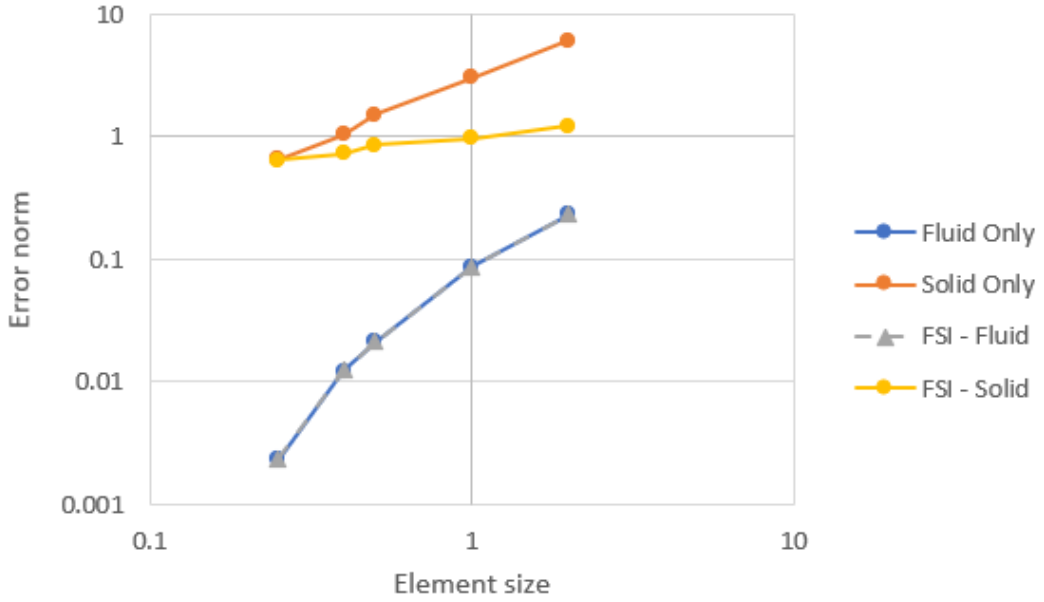

Figure 5.5: Summary of the convergence test cases showing the error norm over various element sizes at $t = 0.5s$. Note that the Fluid Only case and the FSI - Fluid case lie on top of one another showing that the results of those simulations are near identical relative to the other cases at $t = 0.5\,\mathrm{s}$.

5.2 Fluid Only Model with Waves

A Fluid Only model tests the validity of the fluid representing a patch of the ocean surface in the two-dimensional basal plane. Here, the fluid velocity is initialized based on $\nabla \cdot \boldsymbol{u} = s$. Bi-directional periodicity was applied to the domain BCs to account for fluid flow coming in and out the domain at all four boundaries. Equations representing ocean gravity waves were formulated and projected onto the basal plane resulting in Eqs. (5.3) and (5.4),

$$\omega = \sqrt{\frac{g(j^2 + k^2)}{L}} \tag{5.3}$$

and

$$s\,(x,\ y) = \left(\frac{\omega}{L}\sin\left(\frac{2\pi}{L}(jx + ky) - \omega t\right), \frac{\omega}{L}\sin\left(\frac{2\pi}{L}(jx + ky) - \omega t\right)\right), \tag{5.4}$$

where g represents the gravitational acceleration of 9.81 m/s, and j and k represent the wave forcing modes. Table 5.4 shows the parameters used for the simulation.

Table 5.4: Parameters used for Fluid Only simulation of ocean gravity waves.

Final time, T	10 s
Fluid density, ρ_f	1 kg/m^3
Dynamic viscosity, μ	1 Pa s
Drag coefficient,ψ	[0,1]
j	1
k	0
L	60 m
Domain length, L	60 m
Domain width, W	60 m
Element size, h	1 m

At the time of this case study, only skin drag was implemented in the model. The drag coefficient was varied between zero and one, where zero represented no drag effects and one represented maximum drag effects. Figure 5.6 shows the velocity magnitude results of the first five seconds of the simulation, where the wave field enters from the left boundary and exits through the right boundary.

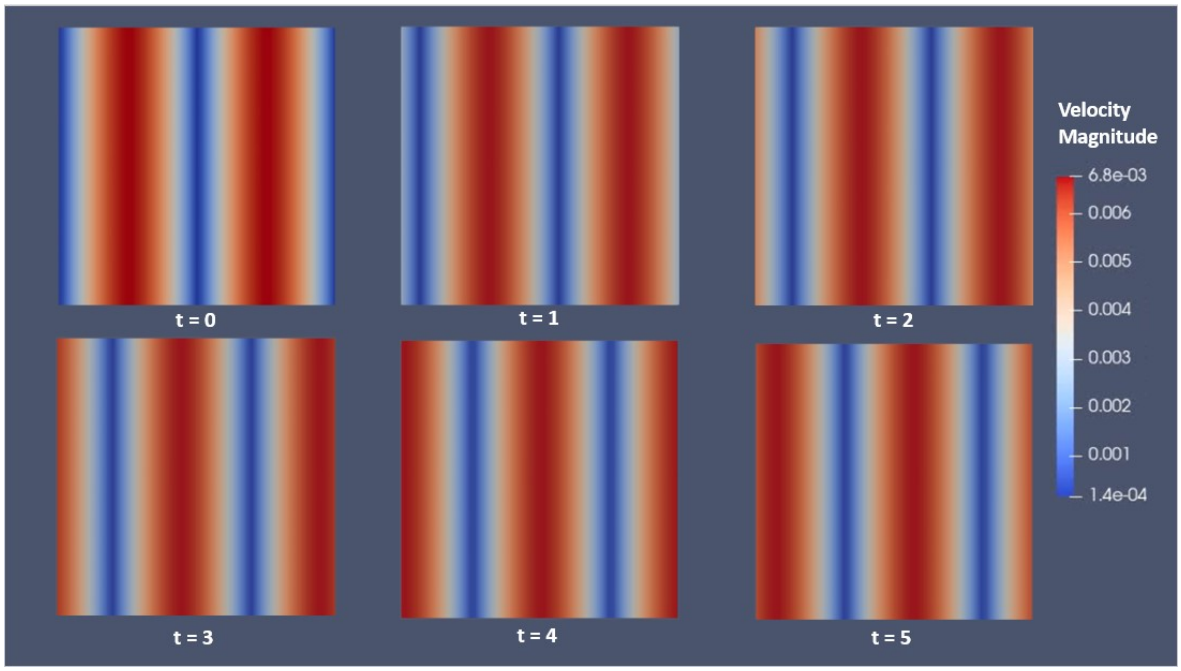

Figure 5.6: Snapshots of the velocity magnitude of the Fluid Only simulation with ocean gravity waves implemented.

Based on the chosen wave forcing modes, the waves enter from the left boundary and exit through the right boundary, remaining continuous along all four boundaries.

To test the drag effects on the fluid, a fictitious Gaussian function 5.5 representing solid

velocity was added to the centre of the domain,

$$f(x, y) = e^{\frac{(x-30)^2-(y-30)^2}{32}}. \tag{5.5}$$

The drag coefficient scales the difference between the solid and fluid velocities and contributes to the forcing in the fluid momentum equation (4.2). Fig. 5.7 shows the velocity magnitude results of the first five seconds of the simulation for a drag coefficient of 0.01.

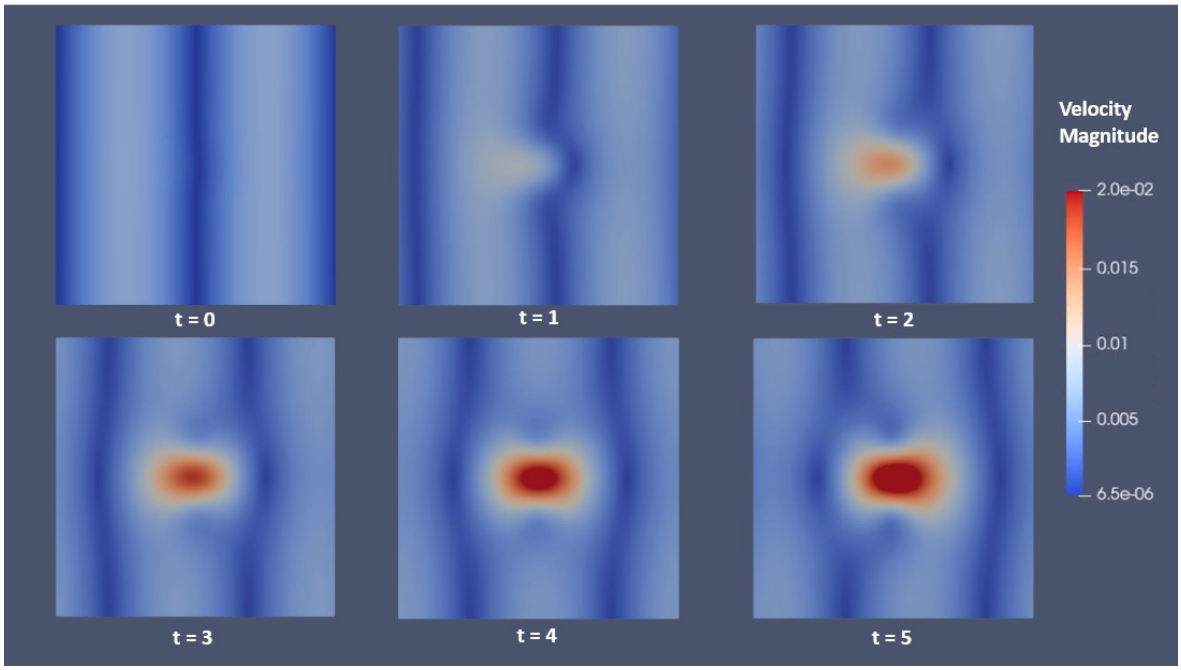

Figure 5.7: Snapshots of the velocity magnitude of the fluid only simulation with a Gaussian function applying drag to the system.

As shown in Fig. 5.7, there is a clear disturbance caused in the waves from the Gaussian function. The results show that the fluid simulation responds accordingly to obstructions/disturbances. It also shows that the fluid model is able to output the desired wave profile.

5.3 Solid Only Model

The solid model can accommodate multiple solids in the modelled domain. Table 5.5 shows the parameters used in the simulation where five solid circular objects were added which were initially pre-stretched in the x-direction and given initial velocities of 0.2 m/s also in the x-direction. The domain had periodicity in both directions.

Table 5.5: Parameters used for Solid Only simulation of multiple solids.

Final time, T	5 s
Solid density, ρ_s	1 kg/m^3
Stabilizing viscosity, μ_{stab}	0.05 Pa s
Bulk modulus, K	20 N/m^2
Shear modulus, G	10 N/m^2
Domain length, L	2 m
Domain width, W	2 m
Element size, h	0.015 625 m

Figures 5.8 and 5.9 show the horizontal and vertical velocities of the solids in the simulated domain respectively. The figures also showcase the periodicity of the domain boundaries. The velocity results are as expected, with the horizontal component rendering an approximate velocity of 0.2 m/s to the right of the domain and some oscillation due to the pre-stretching of the solids. The vertical component shows an approximate velocity of 0 m/s with the same type of oscillation due to the pre-stretching.

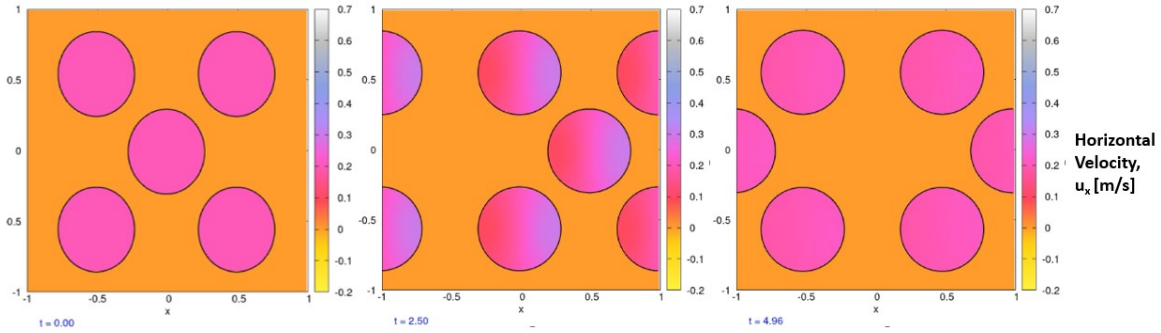

Figure 5.8: Snapshots of the solid velocity in the x-direction.

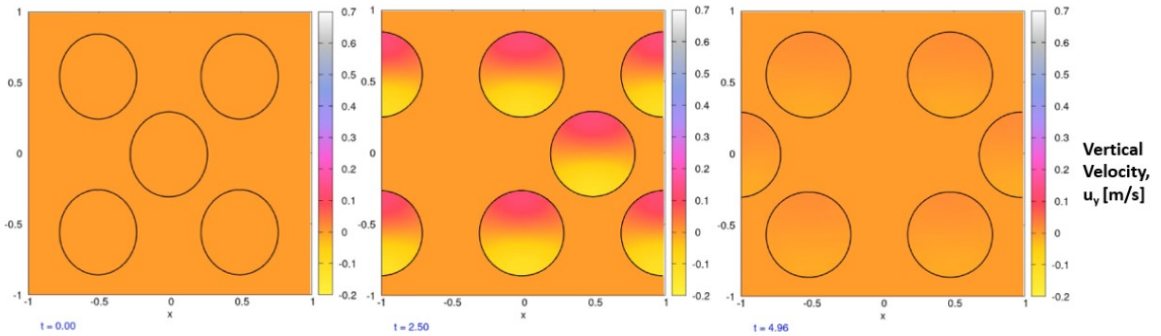

Figure 5.9: Snapshots of the solid velocity in the y-direction

The three stress components of the solid stress state are shown in figures 5.10, 5.11, and 5.12. The results show the stress response of the solids to the pre-stretching initial condition. The

normal stresses show a maximum compression of approximately 0.5 kPa, and the shear stress shows a maximum of ± 0.07 kPa at $t = 2.5$ s. Significant dampening occurs as time passes due to the extra stabilising viscosity added to the system.

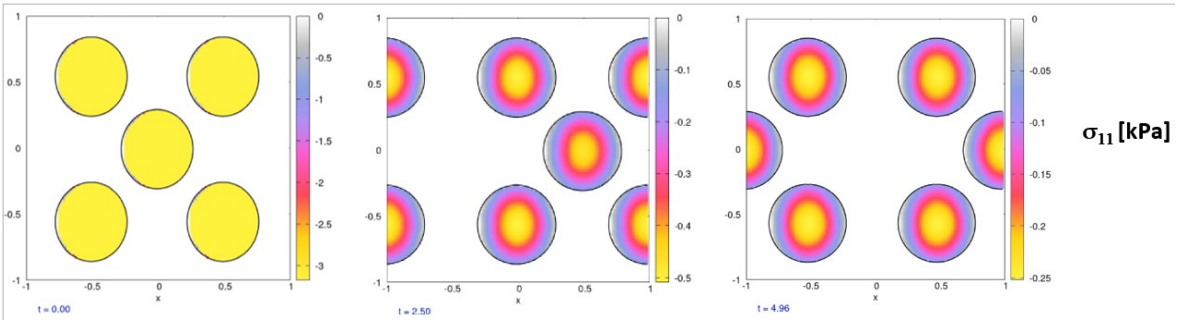

Figure 5.10: Snapshots of the solid stress component σ_{11}.

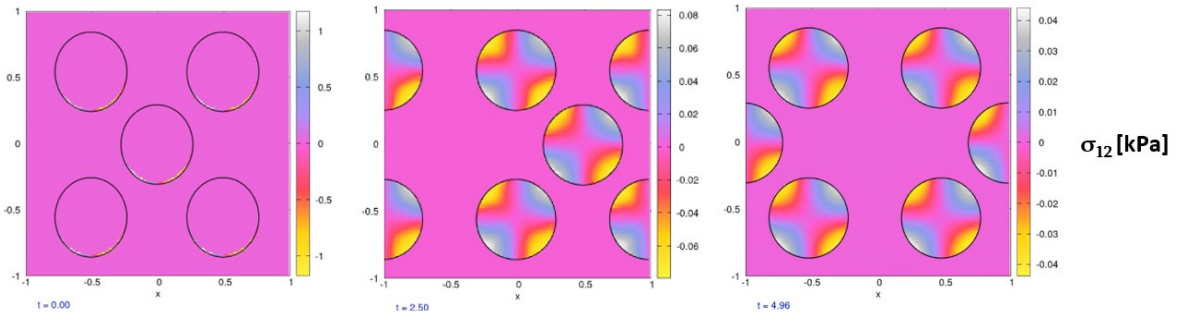

Figure 5.11: Snapshots of the solid stress component σ_{12}.

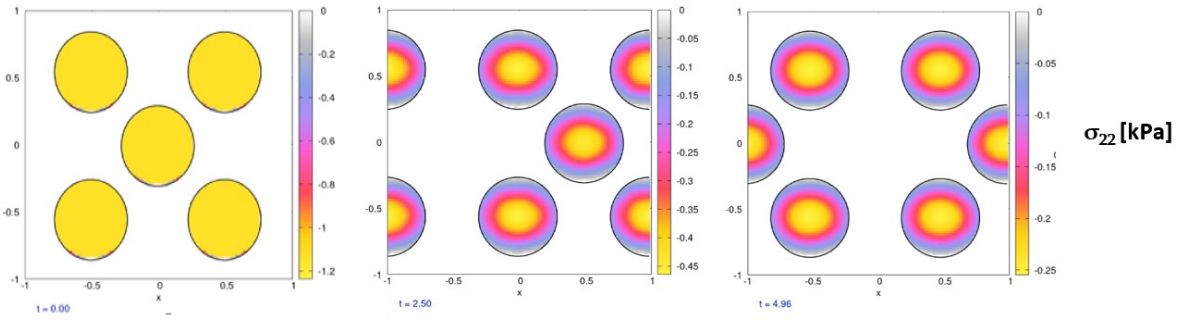

Figure 5.12: Snapshots of the solid stress component σ_{22}.

The results of the stress components show the response to the pre-stretching and are not affected by anything else in the domain such as where the solids cross over the left and right boundaries. It is also shown that the solid model can accommodate multiple solid objects in the simulations.

5.4 Coupled Fluid-Solid Model

This case study shows the coupled system, where the fluid and solid models are iteratively solved and the transfer forces between the solid and fluid constituents is accounted for. Realistic sea ice values were used in this simulation from [21, 22, 28]. Due to the increased stiffness of the ice, the explicit time stepping scheme for the solid domain required smaller time steps than the fluid. To account for the solid model requiring a reduced time step compared to the fluid model, a sub-stepping procedure was introduced for the coupling of the two models. The number of sub-steps required was found by trial and error and scales proportionally with the square-root of the shear modulus, $\sqrt{G}$.

Periodic BCs were applied in both directions and the initial conditions were such that the solids have zero velocity in x- and y- directions and the fluid has ocean gravity wave forcing in x-direction imposed. Three sub-cases will be presented, skin drag of one solid ice floe in grease ice, both skin and form drag of one ice floe in grease ice, and lastly, multiple ice floes in the grease ice.

5.4.1 Skin Drag of One Ice Floe in Grease Ice

For this first case, a reduced, yet still relatively stiff, bulk and shear modulus was used in comparison to the actual sea ice parameters to investigate the model's ability to simulate stiffer material constants. Tab. 5.6 summarises the parameters used for this case. As shown, the bulk and shear moduli are two orders of magnitude lower than the actual values.

Table 5.6: Parameters used for the coupled fluid-structure interaction simulation for the skin drag of one ice floe in grease ice case, taken from Skatulla et al. [39].

Final time	$10\,\mathrm{s}$
Solid density	$918\,\mathrm{kg/m^3}$
Fluid density	$930\,\mathrm{kg/m^3}$
Dynamic viscosity	$50\,\mathrm{Pas}$
Stabilizing viscosity	$\approx 1300\,\mathrm{Pas}$
Bulk modulus	$6 \times 10^4\,\mathrm{Pa}$
Shear modulus	$\approx 3 \times 10^4\,\mathrm{Pa}$
Skin drag coefficient	10^5
Domain length	$60\,\mathrm{m}$
Domain width	$60\,\mathrm{m}$
Element size	$0.5\,\mathrm{m}$
Solid substeps	100

The fluid velocity components are shown in Figs. 5.13 and 5.14. The fluid velocity results

show the response to the wave forcing as well as the solid acting as a floating obstruction in the domain. It is also shown how the skin drag affects the wave propagation over time in the region where the solid is present. This is seen by the delay in the velocity field with respect to the wave forcing in the solid region.

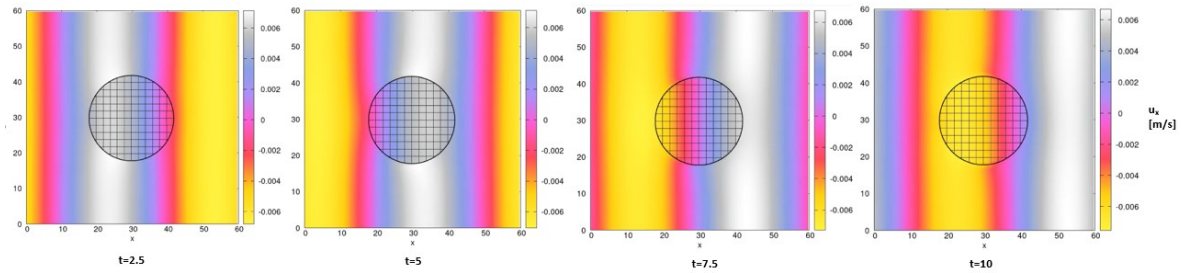

Figure 5.13: Snapshots of the fluid velocity in the coupled FSI case in the x direction, with the reference map overlayed to show the solid region.

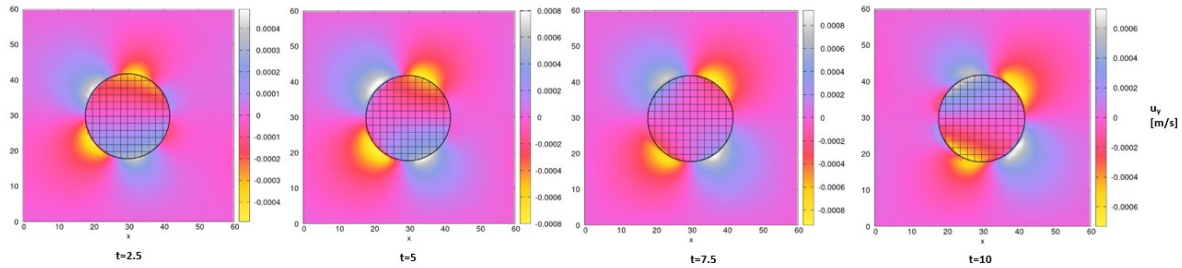

Figure 5.14: Snapshots of the fluid velocity in the coupled FSI case in the y direction, with the reference map overlayed to show the solid region.

The solid velocity components are shown in Figs. 5.15 and 5.16. The results show the effect that the wave forcing has on the solid due to the skin drag force, and confirms the coupling of the fluid and solid models. As the peak and subsequent trough passes through the domain, the solid velocity initially increases ($t = 2.5s$ - $t = 5s$) due to the peak and then slows down and eventually moves in the negative x-direction ($t = 10s$), due to the trough of the wave forcing. The scale in Fig. 5.15 adjusts for the negative direction which is why the background colour of the last snapshot is different from the rest.

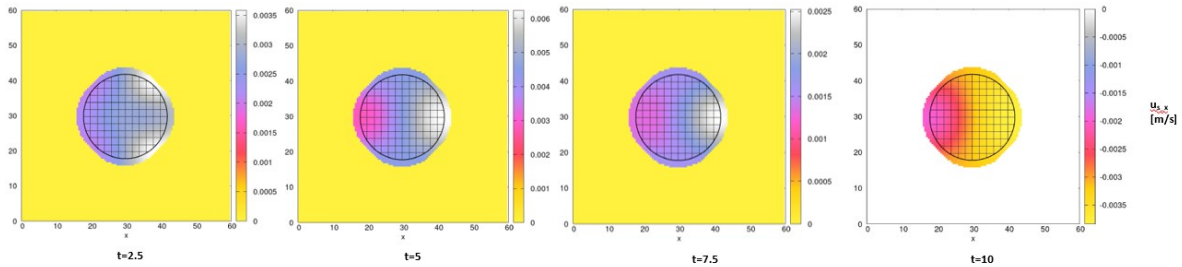

Figure 5.15: Snapshots of the solid velocity in the coupled FSI case in the x-direction.

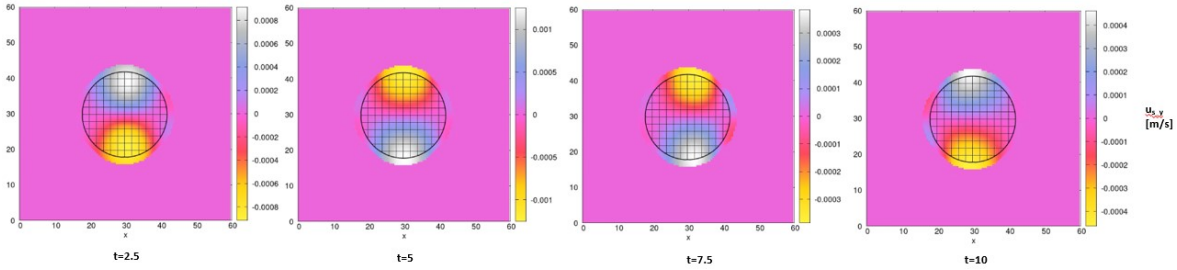

Figure 5.16: Snapshots of the solid velocity in the coupled FSI case in the y-direction.

The solid stress components are shown in Figs. 5.17, 5.18 and 5.19. From the stress results it is clear to see the compression and tension caused by the wave forcing on the solids as it propagates through the domain.

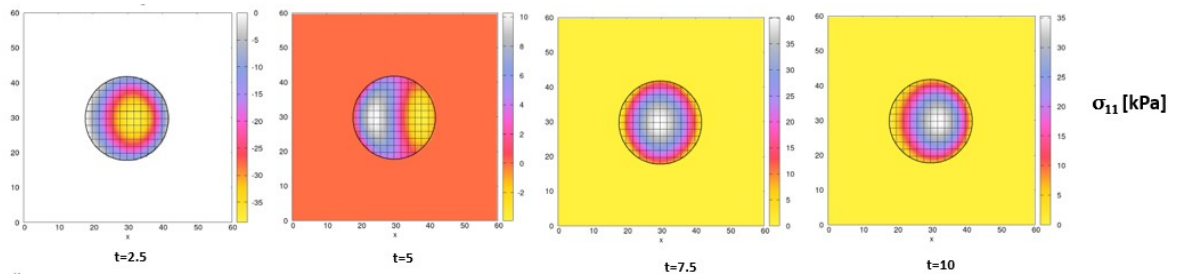

Figure 5.17: Snapshots of the σ_{xx} solid stress component in the coupled FSI case.

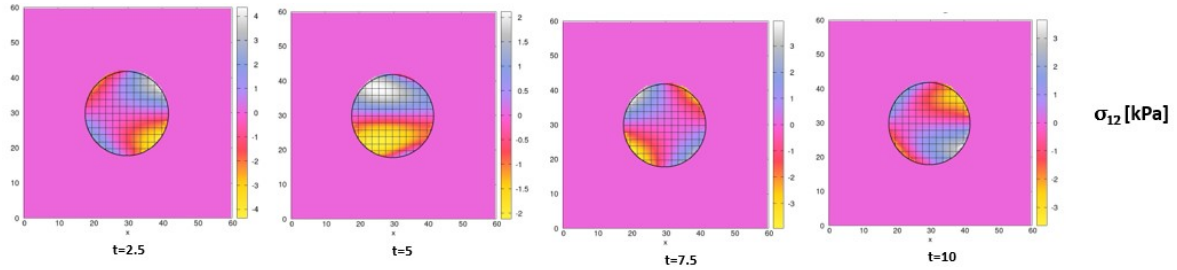

Figure 5.18: Snapshots of the solid shear stress component σ_{xy} in the coupled FSI case.

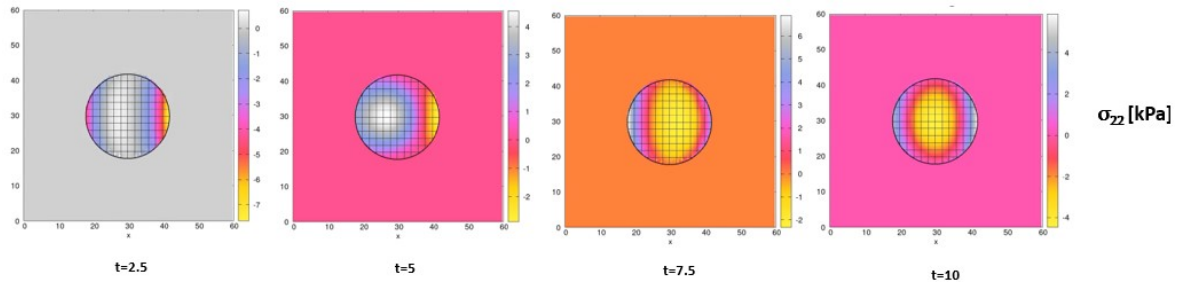

Figure 5.19: Snapshots of the σ_{yy} solid stress component in the coupled FSI case.

5.4.2 Skin and Form Drag of One Ice Floe in Grease Ice

This case uses realistic material properties with the bulk and shear moduli at the correct stiffness which is also in accordance with the values used in Marquart et al. [22]. To account for the stiffer solids, the solid model requires 1000 more time steps per fluid time step. Tab. 5.7 summarises the parameters used for this case. This case also incorporates form drag forcing on the boundary of the solid in addition to the skin drag forcing. With both forcing types, the model is a more realistic representation of sea ice dynamics.

Table 5.7: Parameters used for coupled fluid-structure interaction simulation for the skin and form drag of one ice floe in grease ice case.

Final time	5 s
Solid density	918 kg/m^3
Fluid density	930 kg/m^3
Dynamic viscosity	50 Pas
Stabilizing viscosity	$\approx$ 1300 Pas
Bulk modulus	6×10^6 Pa
Shear modulus	$\approx 3 \times 10^6$ Pa
Skin drag coefficient	10^5
Form drag coefficient	10^3
Domain length	60 m
Domain width	60 m
Element size	0.5 m
Solid substeps	1000

The fluid velocity components are shown in Figs. 5.20 and 5.21. The wave propagation through the solid region is different compared to the previous case, where the solid region allows more deformation to occur in the previous case compared to the current. This is due to the increased stiffness of the solid; it does not undergo as large deformations as the previous case.

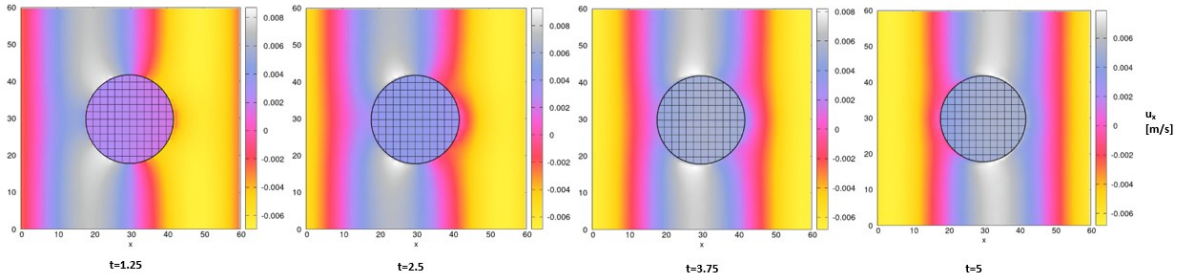

Figure 5.20: Snapshots of the fluid velocity in the coupled FSI case in the x direction.

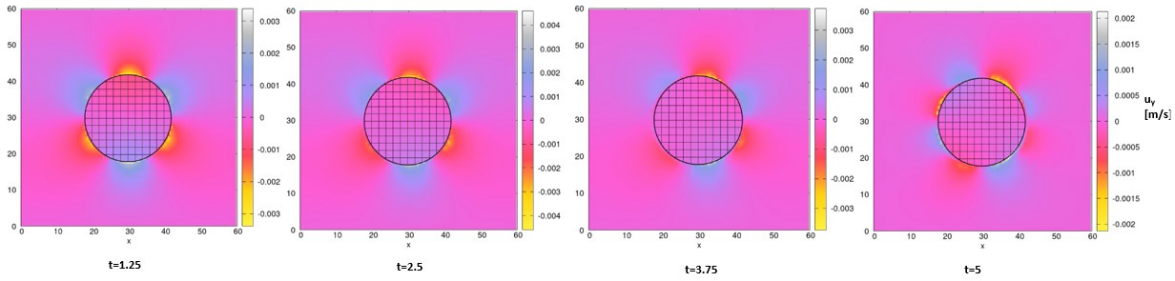

Figure 5.21: Snapshots of the fluid velocity in the coupled FSI case in the y direction.

The solid velocity components are shown in Figs. 5.22 and 5.23. The solid material behaviour is stiffer resulting in less deformation and a more uniform velocity distribution within the solid in the x-direction over time compared to the previous case which showed change within the solid depending on the wave forcing.

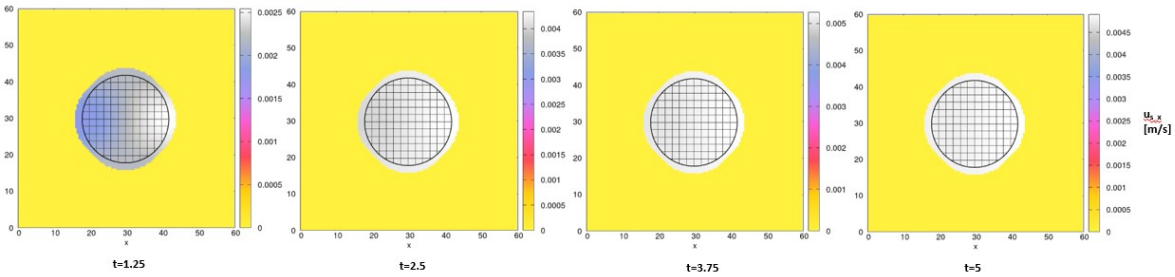

Figure 5.22: Snapshots of the solid velocity in the coupled FSI case in the x-direction.

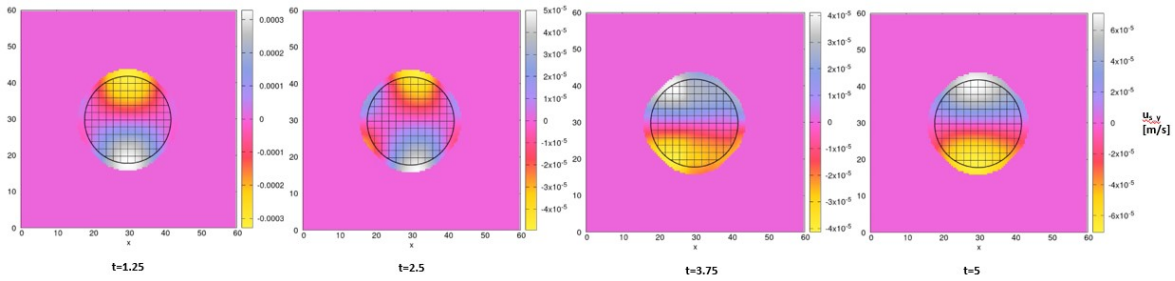

Figure 5.23: Snapshots of the solid velocity in the coupled FSI case in the y-direction.

The stress components are shown in Figs. 5.24, 5.25 and 5.26. The results show the extra circumferential stress due to the form drag around the boundary of the solid floe. The stress is also an order of magnitude higher than the previous case which is expected due to the increased stiffness. The results of the floe stress compare well with results presented in Marquart et al. [22], specifically Fig. 7(a)-(c). The stress profile of the solid floe follows that of the wave forcing profile over time.

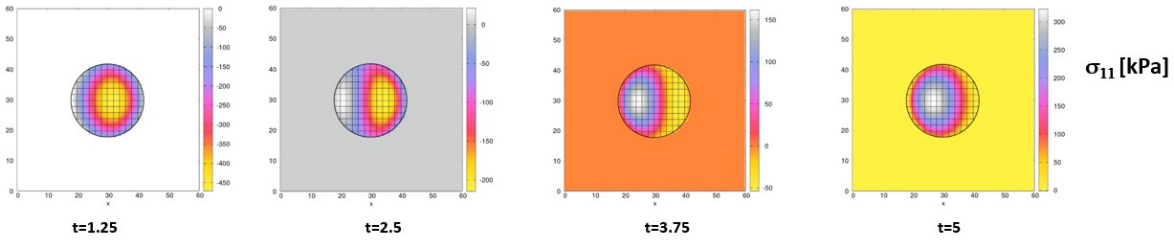

Figure 5.24: Snapshots of the σ_{xx} stress component in the coupled FSI case.

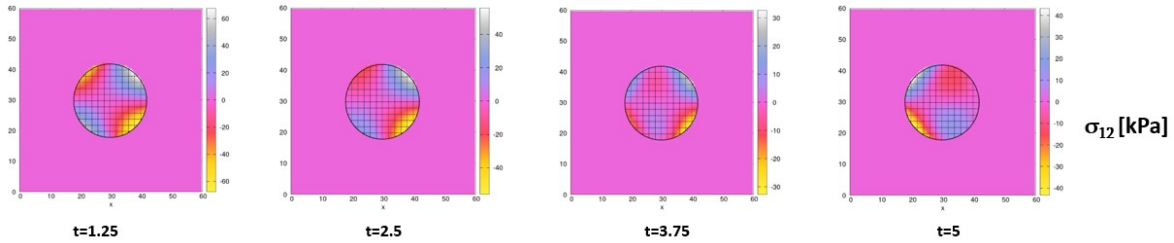

Figure 5.25: Snapshots of the shear stress component σ_{xy} in the coupled FSI case.

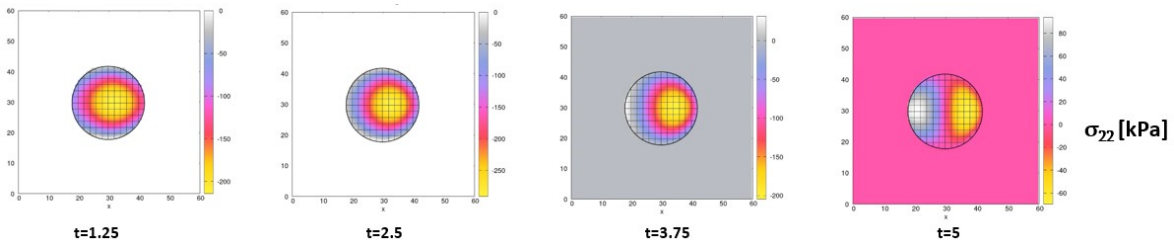

Figure 5.26: Snapshots of the σ_{yy} stress component in the coupled FSI case.

Given the above results which includes skin and form drag, it can therefore be shown that this coupled model can contribute towards a sea ice model with one ice floe present in grease ice. The next case will demonstrate a case with multiple ice floes.

5.4.3 Multiple Ice Floes in the Grease Ice

This final case brings all previous aspects together and also showcases the ability of the model to accommodate multiple solid ice floes in the fluid-like grease ice. In order to make the study more realistic, the ice floes have different diameters and are in a non-symmetric fashion distributed within the domain. Tab. 5.8 summarises the parameters used for this case.

Table 5.8: Parameters used for the coupled fluid-structure interaction simulation of multiple ice floes in grease ice.

Final time	10 s
Solid density	918 kg/m^3
Fluid density	930 kg/m^3
Dynamic viscosity	500 Pas
Stabilizing viscosity	$\approx$ 1300 Pas
Bulk modulus	6×10^6 Pa
Shear modulus	$\approx 3 \times 10^6$ Pa
Skin drag coefficient	10^5
Form drag coefficient	10^3
Domain length	60 m
Domain width	60 m
Element size	0.5 m
Solid substeps	1000

Figs. 5.27 and 5.28 show snapshots of the fluid velocity over 10 s in the x- and y-directions, respectively. The results show the interference that the solid floes have on the wave propagation. There is also a clear indication that the fluid stress is significantly higher in regions where two solids are near to one another/almost colliding. This is also thought to be a possible reason for why the simulations encountered issues when solids came too close together.

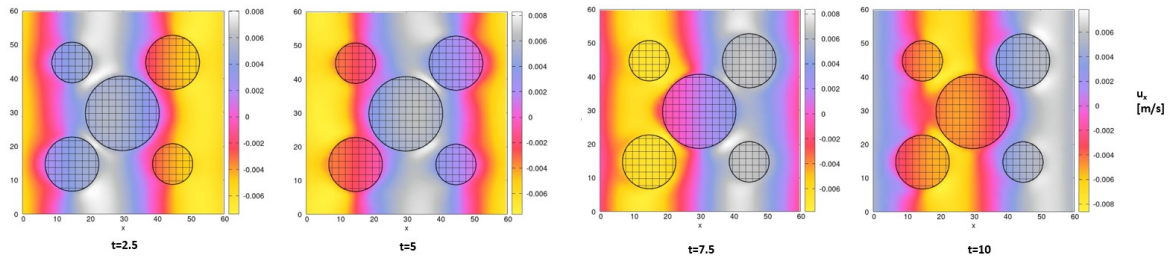

Figure 5.27: Snapshots of the fluid velocity in the coupled multi-solid FSI case in the x-direction, with the reference map overlayed to show the solid regions.

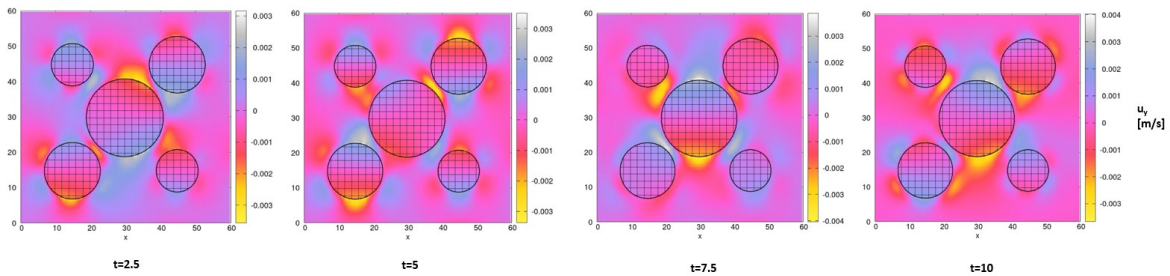

Figure 5.28: Snapshots of the fluid velocity in the coupled multi-solid FSI case in the y-direction, with the reference map overlayed to show the solid regions.

The σ_{11} component of the solid stress is shown in Figure 5.29. The results share similarities with that of the stress in the previous FSI case, with the form drag adding subtle, yet noticeable, stress along the solid circumferences. Each floe experiences different stresses due to the wave forcing at different regions in the domain.

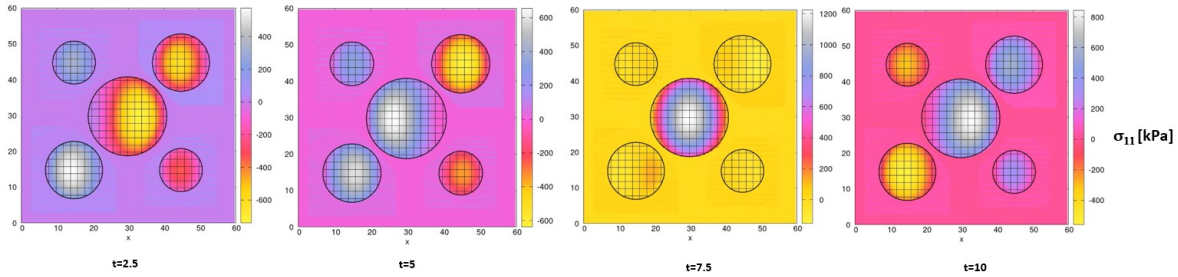

Figure 5.29: Snapshots of the σ_{xx} stress component in the coupled multi-solid FSI case.

With this final case, it has been shown how multiple solid ice floes have been modelled in fluid-like grease ice with realistic sea ice parameters. It was also shown how drag and wave forcing have been incorporated into the model and the effect it has on the dynamics of the system. Incorporating multiple solids into the domain came with little difficulty as it required only adding solid objects with prescribed material parameters into the domain in regions where there were no other solids present.

As shown, this model stands out for several reasons, including its ability to simulate free-standing waves, which many FSI models struggle to do without introducing a numerical wave tank [11, 50]. In addition, many models struggle to encapsulate stiff materials [45, 46], such as sea ice. The solid model has, however, overcome this issue by introducing sub-stepping of the time step allowing for the actual material parameters of sea ice to be used.

Chapter 6

Conclusion and Future Work

The above literature review revealed uncertainties with regards to modelling sea ice and its contribution to the global climate. It indicated a need for small-scale models which will provide a better understanding of Antarctic sea ice dynamics. Therefore, this work shows how using a novel FSI approach which simultaneously solves the solid mechanics, fluid dynamics and the subsequent interactions, may address this gap in the research [22, 37]. This research is important because it contributes to more accurate climate models and forecasts.

6.1 Addressing the Aim and Objectives of Research

The aim of this research was to develop a novel FSI model that can be used to describe sea ice dynamics in the Antarctic MIZ. From the results presented, a small scale model has been developed that has used novel FSI techniques for sea ice dynamics modelling. The model demonstrated satisfactory grid size convergence for all three cases under investigation, namely the Solid Only, Fluid Only and Coupled FSI models.

The main research question was, "How can FSI be used to simulate sea-ice dynamics?". This research has demonstrated a proof of concept which shows the use of FSI and the RMT in simulating sea ice dynamics in a two-dimensional sense. The model accommodates the use of realistic sea ice material parameters with skin and form drag acting on a solitary ice floe and multiple floes in grease ice. The incorporation of waves into the model domain was demonstrated and the interaction of the floes with the waves was analysed.

Four objectives were presented in the research. This research has demonstrated the development of a small-scale two-dimensional FSI model. It was shown that the model can accommodate material parameters that represent ice floes and grease ice and that the solid ice floes are free-floating relative to the domain. The model also implemented wave forcing and drag forcing. The stress and strain rate responses of the dynamics as a result of the wave and drag forcing were analysed.

Significant steps towards a realistic ice floe-grease ice and wave interaction model have been made. As the Froude-Krylov force is missing and as this study has only carried out a plausibility check by qualitatively comparing some of the results with literature, further investigation is required to confirm that this modelling technique can be used to represent sea ice dynamics.

6.2 Recommendations and Future Work

This work serves as a proof of concept for a sea ice dynamics model using the RMT and further improvements can be made. Firstly, a more realistic fluid material law which has a rate dependent viscosity can be incorporated. The current model uses a Newtonian fluid law whereas the grease ice has a more non-linear material behaviour. The solid and fluid laws were chosen to reduce the level of complexity for the masters project.

Secondly, solid-solid collision dynamics can be incorporated into the model by introducing some inelastic collision scheme to the forces between the solids. Friction between the ice floes and the ice floes and grease ice can then also be applied with this scheme. The ice floes can also then undergo some self-adhesion mechanism with the correct prescription of the impact characteristics.

Thirdly, the Froude-Krylov force needs to be incorporated into the sea ice model to accurately represent all types of forcing in the ice. The model can also be extended to be used in larger scale simulations with hundreds of ice floes of more realistic shapes and sizes. Although, this would require more intensive computational power.

Lastly, three-dimensional simulations of sea ice dynamics can be investigated and various wave modes can be assessed. This will also allow for simulating the rafting of ice floes.

Bibliography

[1] A. Alberello, L. Bennetts, P. Heil, C. Eayrs, M. Vichi, K. MacHutchon, et al. "Drift of pancake ice floes in the winter Antarctic marginal ice zone during polar cyclones". In: *Journal of Geophysical Research: Oceans* 125.3 (2020), e2019JC015418.

[2] O. Arzel, T. Fichefet, and H. Goosse. "Sea ice evolution over the 20th and 21st centuries as simulated by current AOGCMs". In: *Ocean Modelling* 12.3-4 (2006), pp. 401–415.

[3] P. Cardiff, A. Karač, P. De Jaeger, H. Jasak, J. Nagy, A. Ivanković, et al. "An open-source finite volume toolbox for solid mechanics and fluid-solid interaction simulations". In: *arXiv preprint arXiv:1808.10736* (2018).

[4] A. J. Chorin. "Numerical solution of the Navier-Stokes equations". In: *Mathematics of computation* 22.104 (1968), pp. 745–762.

[5] A. J. Chorin. "The numerical solution of the Navier-Stokes equations for an incompressible fluid". In: *Bulletin of the American Mathematical Society* 73.6 (1967), pp. 928–931.

[6] J. C. Comiso and F. Nishio. "Trends in the sea ice cover using enhanced and compatible AMSR-E, SSM/I, and SMMR data". In: *Journal of Geophysical Research: Oceans* 113.C2 (2008).

[7] S. C. Doney, V. J. Fabry, R. A. Feely, and J. A. Kleypas. "Ocean acidification: the other CO2 problem". In: *Annual review of marine science* 1 (2009), pp. 169–192.

[8] R. Fogt, A. Sleinkofer, M. Raphael, and M. Handcock. "A Regime Shift in Seasonal Total Antarctic Sea Ice Extent in the 20th Century". In: (2021).

[9] P. S. Foundation. "ctypes — A foreign function library for Python". In: *Python Documentation* (2001-2024).

[10] W. Hibler III. "A dynamic thermodynamic sea ice model". In: *Journal of physical oceanography* 9.4 (1979), pp. 815–846.

[11] L. Huang, K. Ren, M. Li, Ž. Tuković, P. Cardiff, and G. Thomas. "Fluid-structure interaction of a large ice sheet in waves". In: *Ocean Engineering* 182 (2019), pp. 102–111.

[12] E. Hunke and Y. Zhang. "A comparison of sea ice dynamics models at high resolution". In: *Monthly Weather Review* 127.3 (1999), pp. 396–408.

[13] E. C. Hunke and J. K. Dukowicz. "An elastic–viscous–plastic model for sea ice dynamics". In: *Journal of Physical Oceanography* 27.9 (1997), pp. 1849–1867.

[14] *IPCC, 2023: Climate Change 2023: Synthesis Report, summary for Policymakers. Contribution of working groups I, II and III to the Sixth Assessment Report of the Intergovernmental Panel on Climate Change [core writing team, H. lee and J. romero (eds.)]. IPCC, Geneva, Switzerland.* July 2023.

[15] K. Kamrin, C. H. Rycroft, and J.-C. Nave. "Reference map technique for finite-strain elasticity and fluid–solid interaction". In: *Journal of the Mechanics and Physics of Solids* 60.11 (2012), pp. 1952–1969.

[16] A. L. Kohout, M. H. Meylan, and D. R. Plew. “Wave attenuation in a marginal ice zone due to the bottom roughness of ice floes”. In: *Annals of Glaciology* 52.57 (2011), pp. 118–122.

[17] A. Logg, K.-A. Mardal, and G. Wells. *Automated solution of differential equations by the finite element method: The FEniCS book*. Vol. 84. Springer Science & Business Media, 2012.

[18] H. P. L.
bibinitperiod A. Logg. *Solving PDEs in Python - The FEniCS Tutorial Volume I*. CC Attribution, 2017.

[19] N. S. Lovenduski, N. Gruber, and S. C. Doney. “Toward a mechanistic understanding of the decadal trends in the Southern Ocean carbon sink”. In: *Global Biogeochemical Cycles* 22.3 (2008).

[20] T. Maksym. “Arctic and Antarctic Sea ice change: contrasts, commonalities, and causes”. In: *Annual Review of Marine Science* 11 (2019), pp. 187–213.

[21] R. Marquart, A. Bogaers, S. Skatulla, A. Alberello, A. Toffoli, and C. Schwarz. “Small-scale computational fluid dynamics modelling of the wave induced ice floe-grease ice interaction in the Antarctic marginal ice zone”. In: *Cold Regions Science and Technology* 219 (2024), p. 104108.

[22] R. Marquart, A. Bogaers, S. Skatulla, A. Alberello, A. Toffoli, C. Schwarz, et al. “A computational fluid dynamics model for the small-scale dynamics of wave, ice floe and interstitial grease ice interaction”. In: *Fluids* 6.5 (2021), p. 176.

[23] R. A. Massom and S. E. Stammerjohn. “Antarctic sea ice change and variability–physical and ecological implications”. In: *Polar Science* 4.2 (2010), pp. 149–186.

[24] I. Metrikin, S. Løset, N. A. Jenssen, and S. Kerkeni. “Numerical simulation of dynamic positioning in ice”. In: *Marine Technology Society Journal* 47.2 (2013), pp. 14–30.

[25] J. E. Mosig, F. Montiel, and V. A. Squire. “Comparison of viscoelastic-type models for ocean wave attenuation in ice-covered seas”. In: *Journal of Geophysical Research: Oceans* 120.9 (2015), pp. 6072–6090.

[26] C. L. Parkinson, K. Y. Vinnikov, and D. J. Cavalieri. “Evaluation of the simulation of the annual cycle of Arctic and Antarctic sea ice coverages by 11 major global climate models”. In: *Journal of Geophysical Research: Oceans* 111.C7 (2006).

[27] C. L. Parkinson and W. M. Washington. “A large-scale numerical model of sea ice”. In: *Journal of Geophysical Research: Oceans* 84.C1 (1979), pp. 311–337.

[28] F. Paul, C. Schwarz, R. Audh, J. Bluhm, S. Johnson, K. MacHutchon, et al. “Sea ice mechanics”. In: *Computer Methods in Materials Science* 23.3 (2023), pp. 5–54. URL: `https://doi.org/10.7494/cmms.2023.3.0816`.

[29] F. Paul, T. Mielke, C. Schwarz, J. Schröder, T. Rampai, S. Skatulla, et al. “Frazil Ice in the Antarctic Marginal Ice Zone”. In: *Journal of Marine Science and Engineering* 9.6 (2021), p. 647.

[30] L. M. Polvani and K. L. Smith. “Can natural variability explain observed Antarctic sea ice trends? New modeling evidence from CMIP5”. In: *Geophysical Research Letters* 40.12 (2013), pp. 3195–3199.

[31] A. Purich and E. W. Doddridge. “Record low Antarctic sea ice coverage indicates a new sea ice state”. In: *Communications Earth & Environment* 4.1 (2023), p. 314.

[32] M. Rabatel, S. Labbé, and J. Weiss. “Dynamics of an assembly of rigid ice floes”. In: *Journal of Geophysical Research: Oceans* 120.9 (2015), pp. 5887–5909.

[33] D. A. Randall, R. A. Wood, S. Bony, R. Colman, T. Fichefet, J. Fyfe, et al. “Climate models and their evaluation”. In: *Climate change 2007: The physical science basis. Contribution of Working Group I to the Fourth Assessment Report of the IPCC (FAR)*. Cambridge University Press, 2007, pp. 589–662.

[34] L. A. Roach, J. Dörr, C. R. Holmes, F. Massonnet, E. W. Blockley, D. Notz, et al. “Antarctic sea ice area in CMIP6”. In: *Geophysical Research Letters* 47.9 (2020), e2019GL086729.

[35] R. M. Ross, L. B. Quetin, D. G. Martinson, R. A. Iannuzzi, S. E. Stammerjohn, and R. C. Smith. “Palmer LTER: Patterns of distribution of five dominant zooplankton species in the epipelagic zone west of the Antarctic Peninsula, 1993–2004”. In: *Deep Sea Research Part II: Topical Studies in Oceanography* 55.18-19 (2008), pp. 2086–2105.

[36] C. H. Rycroft and J. Wilkening. “Computation of three-dimensional standing water waves”. In: *Journal of Computational Physics* 255 (2013), pp. 612–638.

[37] C. H. Rycroft, C.-H. Wu, Y. Yu, and K. Kamrin. “Reference map technique for incompressible fluid–structure interaction”. In: *Journal of Fluid Mechanics* 898 (2020).

[38] I. Sadrehaghighi, ed. *Multi-Physics Flow & Fluid Structure Interactions (FSI)*. 2.11. CFD Open Series, Jan. 2022. DOI: 10.13140/RG.2.2.19606.86082/7.

[39] S. Skatulla, R. R. Audh, A. Cook, E. Hepworth, S. Johnson, D. C. Lupascu, et al. “Physical and mechanical properties of winter first-year ice in the Antarctic marginal ice zone along the Good Hope Line”. In: *The Cryosphere Discussions* 2021 (2021), pp. 1–35. DOI: 10.5194/tc-2021-209. URL: https://tc.copernicus.org/preprints/tc-2021-209/.

[40] M. Smith and J. Thomson. “Ocean surface turbulence in newly formed marginal ice zones”. In: *Journal of Geophysical Research: Oceans* 124.3 (2019), pp. 1382–1398.

[41] S. Solomon, M. Manning, M. Marquis, D. Qin, et al. *Climate change 2007-the physical science basis: Working group I contribution to the fourth assessment report of the IPCC*. Vol. 4. Cambridge university press, 2007.

[42] V. A. Squire. “Ocean wave interactions with sea ice: A reappraisal”. In: *Annual Review of Fluid Mechanics* 52 (2020), pp. 37–60.

[43] V. A. Squire. “Of ocean waves and sea-ice revisited”. In: *Cold Regions Science and Technology* 49.2 (2007), pp. 110–133.

[44] S. Swart, M. D. du Plessis, A. F. Thompson, L. C. Biddle, I. Giddy, T. Linders, et al. "Submesoscale fronts in the Antarctic marginal ice zone and their response to wind forcing". In: *Geophysical Research Letters* 47.6 (2020), e2019GL086649.

[45] A. Timalsina, G. Hou, and J. Wang. "Computing Fluid-Structure Interaction by the Partitioned Approach with Direct Forcing". In: *Communications in Computational Physics* 21.1 (2017), pp. 182–210.

[46] A. Timalsina, G. Hou, and J. Wang. "Partitioned Computation for Fluid-structure Interaction with Rigid Body Motion". In: *Journal of Advances in Applied Mathematics* 3.1 (2018).

[47] B. Valkov, C. H. Rycroft, and K. Kamrin. "Eulerian method for multiphase interactions of soft solid bodies in fluids". In: *Journal of Applied Mechanics* 82.4 (2015), p. 041011.

[48] M. Vichi. "A statistical definition of the Antarctic marginal ice zone". In: *The Cryosphere Discussions* 2021 (2021), pp. 1–23. DOI: 10.5194/tc-2021-307. URL: https://tc.copernicus.org/preprints/tc-2021-307/.

[49] P. Wadhams. *Ice in the Ocean*. CRC Press, 2000.

[50] C. Wang, J. Wang, C. Wang, Z. Wang, and Y. Zhang. "Numerical Study on Wave–Ice Floe Interaction in Regular Waves". In: *Journal of Marine Science and Engineering* 11.12 (2023), p. 2235.

[51] J. Zhang and W. Hibler III. "On an efficient numerical method for modeling sea ice dynamics". In: *Journal of Geophysical Research: Oceans* 102.C4 (1997), pp. 8691–8702.

Appendix A

A.1 Scheduling

The following page shows a detailed timeline of the proposed research from the beginning of January 2022 until the end of December 2023. The model setup stage was prolonged by an extra 6 months and incurred in the simulation cases and thesis write up phases. Overall the schedule was two months out of sync with the realistic timeline of events.

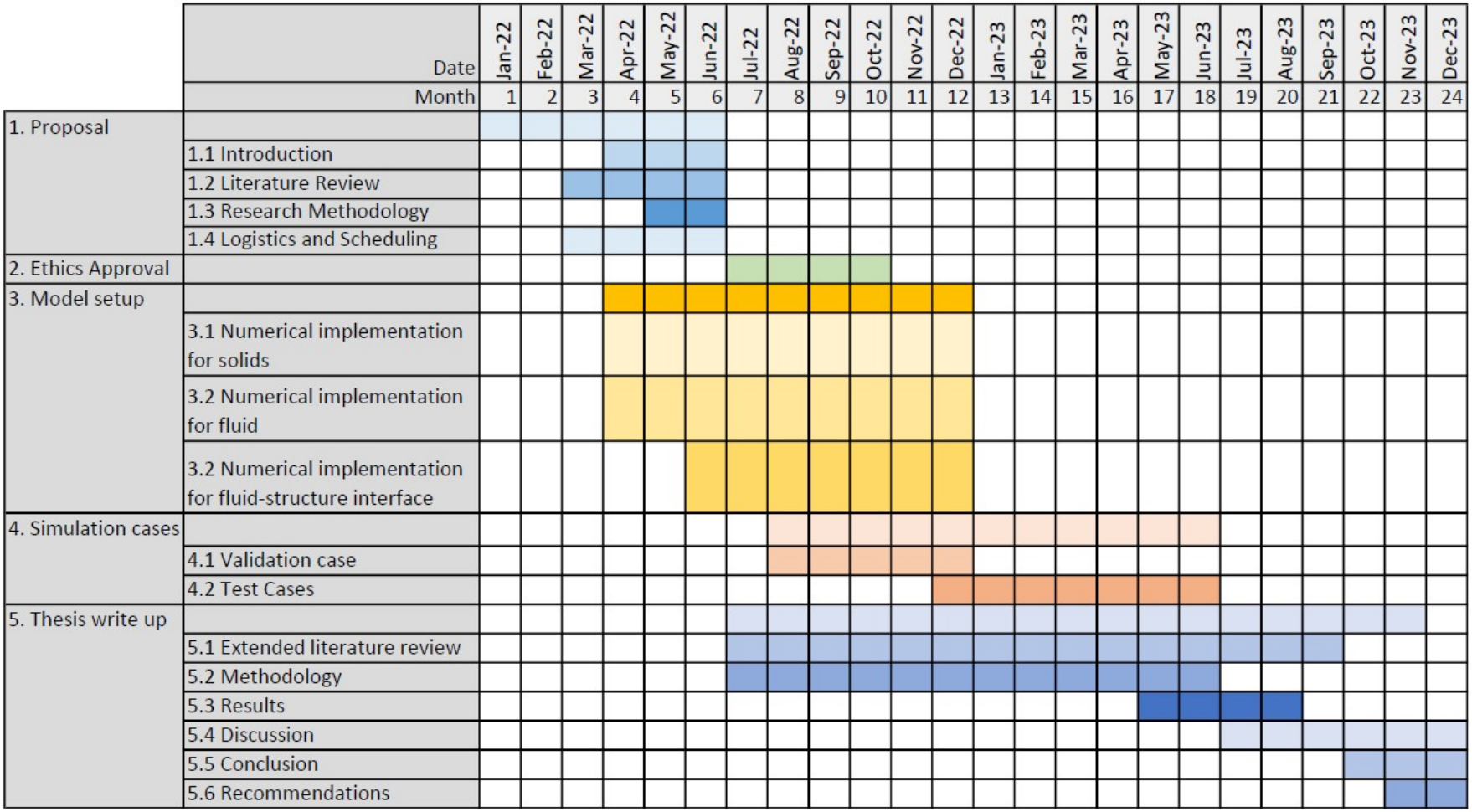

Figure A.1: Gantt Chart showing a timeline of tasks to be completed.

Appendix B

B.1 Weak Forms

Strong form of reference map field advection equation:

$$\frac{\partial \boldsymbol{\xi}}{\partial t} + (\boldsymbol{u} \cdot \boldsymbol{\nabla})\, \boldsymbol{\xi} = \mathbf{0} \tag{1}$$

Multiplying by test function ψ and integrating over each term:

$$\int \left(\frac{\partial \boldsymbol{\xi}}{\partial t} + (\boldsymbol{u} \cdot \boldsymbol{\nabla})\, \boldsymbol{\xi} \right) \cdot \boldsymbol{\psi} d\boldsymbol{x} = \int (\mathbf{0}) \cdot \boldsymbol{\psi} d\boldsymbol{x} \tag{2}$$

$$\int \left(\frac{\partial \xi}{\partial t} \right) \cdot \boldsymbol{\psi} d\boldsymbol{x} + \int ((\boldsymbol{u} \cdot \boldsymbol{\nabla})\, \boldsymbol{\xi}) \cdot \boldsymbol{\psi} d\boldsymbol{x} = 0 \tag{3}$$

Strong form of momentum equation:

$$\rho \left(\frac{\partial u}{\partial t} + (u \cdot \nabla)\, u \right) = \nabla \cdot \sigma \tag{4}$$

Multiplying by test function ψ and integrating over each term:

$$\int \rho \left(\frac{\partial u}{\partial t} + (u \cdot \nabla)\, u \right) \cdot \boldsymbol{\psi} d\boldsymbol{x} = \int (\nabla \cdot \sigma) \cdot \boldsymbol{\psi} d\boldsymbol{x} \tag{5}$$

$$\int_\Omega \rho \left(\frac{\partial u}{\partial t} + (u \cdot \nabla)\, u \right) \cdot \boldsymbol{\psi} d\boldsymbol{x} = \int_\Omega (\sigma : \nabla \boldsymbol{\psi}) d\boldsymbol{x} - \int_{\partial\Omega} \sigma \cdot \hat{n} \cdot \boldsymbol{\psi} d\boldsymbol{x} \tag{6}$$

B.2 Convergence Tests

The L^2 error norms were normalised against the domain size for a precise comparison between the grid resolutions using the following,

$$E_{conv} = \sqrt{\frac{1}{A} \int_\Omega ||\boldsymbol{u} - \boldsymbol{u}_{ref}||^2 d\boldsymbol{x}}, \tag{7}$$

taken from [37], where $A = 60 \times 60$ is the area of the domain, $\boldsymbol{u}_{ref}$ is the reference simulation field, and $\boldsymbol{u}$ is the coarse simulation field. Fig. B.1 shows the relationship between the normalised error norm and element size of the grid for all test cases at $t = 0.5\,\text{s}$. Note that the Fluid Only case and the FSI - Fluid case lie on top of one another showing that the results of those simulations are near identical relative to the other cases at $t = 0.5\,\text{s}$. This shows, once again, that the model converges at a rate of h^2 and that the convergence results are in accordance with the convergence results of [37] (shown in Appendix B of [37]).

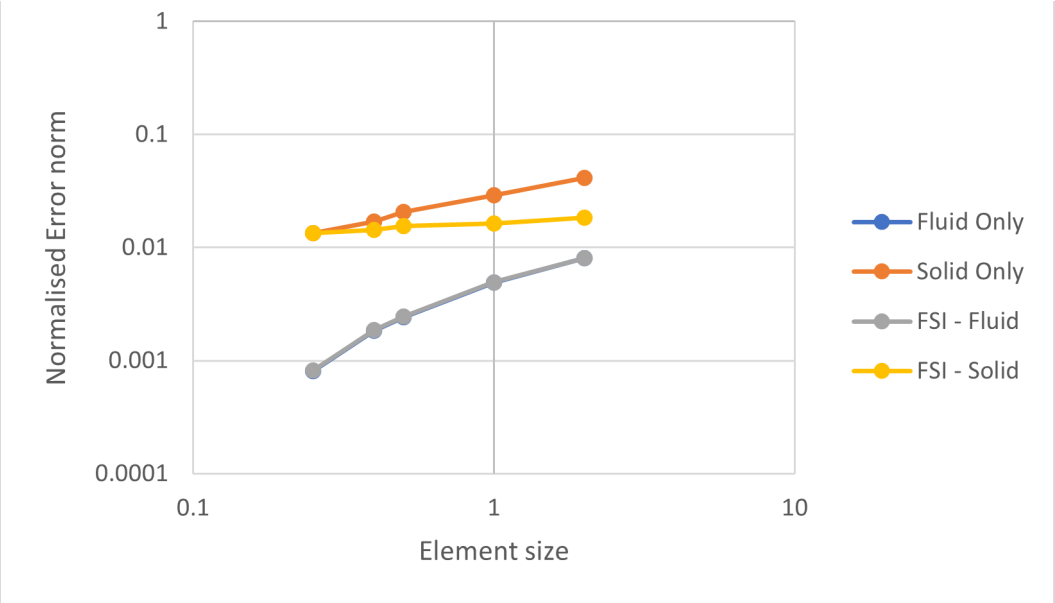

Figure B.1: Summary of the convergence test cases showing the normalised error norm over various element sizes at $t = 0.5s$.

B.3 Model Code

The results from this thesis was created using a code that was developed from scratch and implemented with FEniCS. The code files can be found using this GitLab repository: https://gitlab.com/abogaers/reference-map-fenics.git. Refer to Fig. 4.1 for the breakdown of code files and functions.